

Analytical parametrization of self-consistent polycrystal mechanics: Fast calculation of upper mantle anisotropy

Neil J. Goulding,¹ Neil M. Ribe,² Olivier Castelnau,³ Andrew M. Walker⁴
and James Wookey¹

¹School of Earth Sciences, University of Bristol, Wills Memorial Building, Queen's Road, Bristol BS8 1RJ, United Kingdom. E-mail: ng12245@bristol.ac.uk

²Lab FAST, Univ Paris-Sud/CNRS, Bat 502, Campus Univ, Orsay F-91405, France

³Lab PIMM, CNRS, Arts et Métiers ParisTech, 151 Bd de l'Hopital, Paris F-75013, France

⁴School of Earth and Environment, University of Leeds, Leeds LS2 9JT, United Kingdom

Accepted 2015 July 19. Received 2015 June 26; in original form 2014 December 5

SUMMARY

Progressive deformation of upper mantle rocks via dislocation creep causes their constituent crystals to take on a non-random orientation distribution (crystallographic preferred orientation or CPO) whose observable signatures include shear-wave splitting and azimuthal dependence of surface wave speeds. Comparison of these signatures with mantle flow models thus allows mantle dynamics to be unraveled on global and regional scales. However, existing self-consistent models of CPO evolution are computationally expensive when used with 3-D and/or time-dependent convection models. Here we propose a new method, called ANPAR, which is based on an analytical parametrization of the crystallographic spin predicted by the second-order (SO) self-consistent theory. Our parametrization runs $\approx 2\text{--}6 \times 10^4$ times faster than the SO model and fits its predictions for CPO and crystallographic spin with a variance reduction >99 per cent. We illustrate the ANPAR model predictions for the deformation of olivine with three dominant slip systems, (010)[100], (001)[100] and (010)[001], for three uniform deformations (uniaxial compression, pure shear and simple shear) and for a corner-flow model of a spreading mid-ocean ridge.

Key words: Mantle processes; Creep and deformation; Seismic anisotropy.

1 INTRODUCTION

Seismic anisotropy observed in Earth's upper mantle is typically explained by the partial alignment of the lattices of the constituent olivine and pyroxene crystals caused by deformation associated with mantle convection (e.g. Nicolas & Christensen 1987; Silver 1996; Long & Becker 2010). Because each crystal is elastically anisotropic, this non-random distribution of crystallographic directions (called a crystallographic preferred orientation, or CPO) will impart elastic anisotropy to the bulk material. The seismically observable consequences of this anisotropy include shear-wave birefringence or 'splitting' (e.g. Crampin 1984; Silver & Chan 1991) and the azimuthal dependence of surface-wave speeds (e.g. Montagner & Tanimoto 1991). Simulation of the development of CPO in models of mantle deformation, and comparison of this with seismic observations of the Earth, allow mantle dynamics to be unraveled on global (e.g. Becker *et al.* 2012) and regional scales (e.g. Long 2013). However, these simulations are computationally challenging when performed for time-dependent models of mantle convection or at the high spatial resolution needed for finite frequency simulation of seismic wave propagation. Here we

describe an accurate and computationally efficient alternative to existing methods for the simulation of CPO development in the upper mantle.

The principal cause of CPO and seismic anisotropy in the mantle is the progressive deformation experienced by mantle rocks as they participate in the global convective circulation. Under appropriate conditions of stress, temperature, and grain size, olivine and pyroxene crystals deform via dislocation creep, whereby internal dislocations move through the crystal to accommodate strain. The dislocations move on crystallographic planes and in directions set by the crystal structure, and the combination of a plane and direction define the limited number of slip systems available to allow the crystal to deform. Deformation of this type constrains the crystallographic axes to rotate relative to a fixed external reference frame, much as a tilted row of books on a shelf rotates when one pushes down on it. Because crystals with different orientations rotate at different rates, the overall distribution of orientations evolves with time in a way that reflects both the geometry of the slip systems and the character of the imposed deformation.

Because CPO and seismic anisotropy are so directly linked to progressive deformation, observations of seismic anisotropy have

the potential to constrain the pattern of convective flow in the mantle. Realizing this potential, however, requires a reliable polycrystal mechanics model that can predict how the individual crystals in an aggregate deform and rotate in response to an imposed macroscopic stress or strain rate. Three broad classes of polycrystal models have been proposed to date.

The first class comprises the full-field models. In these, the polycrystal is treated explicitly as a spatially extended body, and the stress and strain within it are field variables that vary continuously as a function of position. Full-field models allow the stress and strain to vary both among and within individual grains in a physically realistic way. This approach can be implemented as a finite element problem (e.g. Sarma & Dawson 1996; Kanit *et al.* 2003) or, more efficiently, using a method based on fast Fourier transforms (Moulinec & Suquet 1998; Lebensohn 2001; Suquet *et al.* 2012). Predictions from full-field models agree remarkably well with laboratory experiments (Grennerat *et al.* 2012) and analytical results available for simple cases (Lebensohn *et al.* 2011). However, their great computational expense makes them too slow (by many orders of magnitude) for routine use in convection calculations.

This disadvantage is overcome to some extent by so-called ‘homogenization’ models, in which the detailed spatial distribution of the grains is ignored and the aggregate is treated as a finite number of grains with different orientations and material properties. In this mean-field approach compatibility of stress and strain equilibrium is not enforced between spatially contiguous grains, but rather between each grain and a ‘homogeneous effective medium’ defined by the average of all the other grains. For viscoplastic behaviours as considered here, a well-known member of this class makes use of the so-called ‘tangent’ anisotropic scheme of Molinari *et al.* (1987) and Lebensohn & Tome (1993). In this model the local stress and strain rate tensors vary among the grains. In the geophysical literature this approach is generally known as the viscoplastic self-consistent (VPSC) model, and we use this name for this first-order approximation. The VPSC model has been widely used in solid-earth geophysics including studies of CPO development in the upper mantle (e.g. Wenk *et al.* 1991; Tommasi *et al.* 1999, 2000, 2009; Wenk & Tomé 1999; Mainprice *et al.* 2005; Bonnin *et al.* 2012; Di Leo *et al.* 2014), the transition zone (Tommasi *et al.* 2004), in the lowermost mantle (Wenk *et al.* 2006; Merkel *et al.* 2007; Wenk *et al.* 2011; Mainprice *et al.* 2008; Walker *et al.* 2011; Dobson *et al.* 2013; Nowacki *et al.* 2013; Amman *et al.* 2014; Cottaar *et al.* 2014), in the inner core (e.g. Wenk *et al.* 2000; Deguen *et al.* 2011; Lincot *et al.* 2015), or in ice (Castelnau *et al.* 1996, 1997). However, as noted by Masson *et al.* (2000), there is an inconsistency in the common first-order VPSC approach in the definition of the stress localization tensor, leading to an inaccurate estimation of the effective rheology for highly anisotropic viscoplastic polycrystals such as olivine (Detrez *et al.* 2015).

More recently, an improved ‘second order’ (SO) self-consistent homogenization scheme has been proposed by Ponte Castañeda (2002). In the SO model the stress and strain rate varies among grains with the same orientation and physical properties, and these fluctuations are used to derive the effective polycrystal behaviour. As a result, its predictions of quantities such as the effective average stress in the aggregate are much more accurate than those of simpler homogenization schemes (Lebensohn *et al.* 2007; Castelnau *et al.* 2008). Recent examples of the application of the SO approach to olivine deformation are provided by Castelnau *et al.* (2008, 2009, 2010) and Raterron *et al.* (2014).

While the physical self-consistency of the SO and simpler VPSC models is appealing, both are computationally expensive when ap-

plied to typical mantle minerals deforming by dislocation creep. The reason is the strongly nonlinear rheology of such minerals, which makes it necessary to use iterative methods to solve the equations of stress compatibility among the large number ($\sim 10^3$ – 10^4) of grains required to represent the polycrystal. Moreover, the number of iterations required at each deformation step increases rapidly as the CPO becomes progressively more strongly anisotropic. These difficulties render the VPSC and SO models unsuitable for calculations of evolving CPO in complex time-dependent mantle flow fields, unless powerful computer capacity and elaborate computation strategies are used. Indeed, because of these computational constraints, none of the studies referenced above make use of the VPSC or SO approaches to directly compute the elasticity on a fine spatial scale (suitable for finite frequency forward modelling of the seismic wave field) from a time-varying description of mantle flow. Instead various approximations are used, such as limiting the calculation to selected ray-theoretical paths (Blackman *et al.* 2002; Nowacki *et al.* 2013; Di Leo *et al.* 2014), interpolating the calculated elasticity (Bonnin *et al.* 2012), or simplifying the model of mantle flow (Raterron *et al.* 2014).

A final degree of physical simplicity and computational efficiency is reached in models of the ‘kinematic’ class, which are based on either an analytical expression for the deformation-induced rate of crystallographic rotation (Ribe & Yu 1991; Kaminski & Ribe 2001; Kaminski *et al.* 2004) or on a simple relationship between finite strain and the expected CPO (Muhlhaus *et al.* 2004; Lev & Hager 2008). One example, the DRex model (Kaminski & Ribe 2001; Kaminski *et al.* 2004) has been widely used to predict CPO and seismic anisotropy from flow models (e.g. Lassak *et al.* 2006; Conder & Wiens 2007; Becker 2008; Long & Becker 2010; Faccenda & Capitanio 2012, 2013; Faccenda 2014). Kinematic models are computationally 10–100 times faster than homogenization models, and predict very similar CPO. However, the physical principle underlying the expression for the spin is *ad hoc*, and has not yet been adequately justified. Moreover, because the kinematic approach does not account explicitly for stress compatibility among grains, it cannot be used to predict rheological properties of a deforming aggregate.

In view of the above limitations, it would clearly be desirable to have a polycrystal model that combines the physical rigour of the self-consistent approach with a much lower computational cost. The aim of this paper is to derive such a model. For purposes of illustration, we consider the case of a pure olivine polycrystal (dunite), a relevant (albeit simplified) representation of the mineralogy of the upper ≈ 400 km of Earth’s mantle. Our approach is to examine in detail the predictions of the SO model for dunites subject to different kinds of deformation, and to extract from those predictions a simple parametrization that can be expressed analytically. The active slip systems of mantle olivine are believed to vary with temperature, pressure and hydrogen content (e.g. Jung & Karato 2001; Cordier *et al.* 2002; Mainprice *et al.* 2005). In order to reduce the parameter space that we need to consider, we limit ourselves to the three dominant slip systems relevant to deformation under anhydrous upper mantle conditions: (010)[100], (001)[100] and (010)[001]. However, we allow the relative importance of these three slip systems to vary and, as discussed below, these slip systems include the most important ones under mantle conditions down to 410 km (Castelnau *et al.* 2010; Raterron *et al.* 2014).

The most important prediction of the SO model is the crystallographic spin \dot{g} as a function of the crystal’s orientation g , which is what controls the evolution of CPO. Accordingly, this paper focusses on the task of deriving an analytical parametrization of \dot{g}

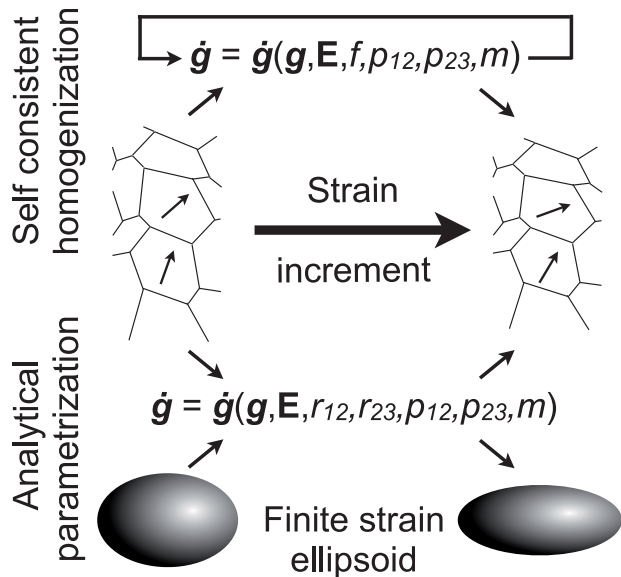


Figure 1. Schematic comparison of the analytical approach and homogenization methods for a single strain increment. Using SO to calculate the spin, $\dot{\mathbf{g}}$, for the n th grain and update its orientation, \mathbf{g} , requires knowledge of the strain, and thus spin, of all other crystals in the aggregate necessitating an expensive self-consistent solution. Our analytical approach replaces this information with a record of previous deformation stored as an auxiliary finite strain ellipsoid. This, combined with a handful of other parameters, A , enables rapid calculation of the spin.

that agrees with the SO model predictions. We first note that the total spin $\dot{\mathbf{g}}$ is the sum of spins $\dot{\mathbf{g}}^{[s]}$ due to the activities of each of the slip systems $s = 1, 2, \dots, S$ within the crystals. We then derive an analytical expression for $\dot{\mathbf{g}}^{[s]}$ that depends on the crystal's orientation, the macroscopic strain rate tensor (SRT), the already existing texture and the parameters that characterize the rheology of the slip systems. This expression is then compared, for each slip system separately, with the spins $\dot{\mathbf{g}}^{[s]}(\mathbf{g})$ predicted by the SO model for an aggregate of crystals with several simultaneously active slip systems ($S > 1$). Remarkably, we find that the analytical expression for $\dot{\mathbf{g}}^{[s]}$ matches the SO prediction exactly for each slip system s , to within a set of amplitudes A_{ijkl} that can be determined by least-squares fitting. We uncover surprising symmetries that reduce the number of independent non-zero components of the 'spin' tensor \mathbf{A} from 25 to just 2. Finally, we use full SO solutions to determine how these coefficients depend on the relative strengths of the slip systems and on the finite strain experienced by the aggregate.

For irrotational, time-independent deformation, the finite strain ellipsoid (FSE) has the same shape and orientation as the virtual ellipsoid generated by the instantaneous global SRT. In this simplified case, we show that we require only one amplitude. However, when the two ellipsoids are not aligned (see Fig. 1), an extra amplitude is required. We show that predictions of evolving CPO using these analytical parametrizations (which we call ANPAR) are indistinguishable from those of the SO model, and cost only ≈ 0.01 per cent as much time to compute.

2 THEORETICAL PRELIMINARIES

We begin by reviewing how the orientation and internal deformation of crystals in an aggregate are described mathematically, using the particular case of olivine as an example.

2.1 Crystal orientation and orientation distribution

Consider an aggregate comprising a large number N of olivine crystals deforming by dislocation creep. When the aggregate as a whole is subject to a given macroscopic deformation, its constituent crystals respond by deforming via internal shear on a small number S of 'slip systems'. Each slip system $s = 1, 2, \dots, S$ is defined by a unit vector $\mathbf{n}^{[s]}$ normal to the slip (glide) plane and a unit (Burgers) vector $\mathbf{l}^{[s]}$ parallel to the slip direction. In this study we assume that olivine has three dominant slip systems (010)[100], (001)[100] and (010)[001], corresponding to the indices $s = 1, 2$, and 3, respectively.

The degree of anisotropy of an aggregate can be described by specifying for each crystal the three Eulerian angles $(\phi, \theta, \psi) \equiv \mathbf{g}$ that describe its orientation relative to fixed external axes. The definition of these angles that we use is shown in Fig. 2, following Bunge's (1982) convention. The associated matrix of direction cosines a_{ij} is

$$a_{ij}(\mathbf{g}) = \begin{pmatrix} c\phi c\psi - s\phi s\psi c\theta & s\phi c\psi + c\phi s\psi c\theta & s\psi s\theta \\ -c\phi s\psi - s\phi c\psi c\theta & -s\phi s\psi + c\phi c\psi c\theta & c\psi s\theta \\ s\phi s\theta & -c\phi s\theta & c\theta \end{pmatrix}, \quad (1)$$

where c and s indicate the cosine and sine, respectively, of the angle immediately following. The quantity a_{ij} is the cosine of the angle between the crystallographic axis i and the external axis j .

In the limit as the number of grains $N \rightarrow \infty$, the distribution of their orientations can be described by a continuous 'orientation distribution function' (ODF) $f(\mathbf{g}, t)$, defined such that $f(\mathbf{g}, t)d\mathbf{g}$ is the volume fraction of crystals with orientations between \mathbf{g} and $\mathbf{g} + d\mathbf{g}$ at time t . For crystals with triclinic symmetry, the volume of the space of Eulerian angles ('Euler space') required to include all possible orientations is $\phi \in [0, 2\pi]$, $\theta \in [0, \pi]$, $\psi \in [0, 2\pi]$. For olivine, which is orthorhombic, it is sufficient to work in a reduced space (so-called 'irreducible space') $\phi \in [0, \pi]$, $\theta \in [0, \pi]$, $\psi \in [0, \pi]$, as the entire Euler space can be retrieved from the irreducible space by symmetry operations. The condition that the total volume fraction of crystals with all possible orientations is unity is then

$$\int f(\mathbf{g}, t)d\mathbf{g} \equiv \int_0^\pi \int_0^\pi \int_0^\pi f(\mathbf{g}, t) d\phi d\psi d\theta \sin\theta = 1, \quad (2)$$

which implies that $f = (2\pi^2)^{-1} \equiv f_0$ for an isotropic orientation distribution.

2.2 Kinematics of intracrystalline slip

The time evolution of the ODF is governed by the equation (Clement 1982)

$$0 = \frac{\partial f}{\partial t} + \nabla \cdot (\dot{\mathbf{g}}f) \equiv \frac{\partial f}{\partial t} + \frac{\partial}{\partial \phi}(\dot{\phi}f) + \frac{\partial}{\partial \psi}(\dot{\psi}f) + \frac{1}{\sin\theta} \frac{\partial}{\partial \theta}(\dot{\theta} \sin\theta f), \quad (3)$$

where $(\dot{\phi}, \dot{\theta}, \dot{\psi}) \equiv \dot{\mathbf{g}}$ is the rate of change of the orientation ('spin') of an individual crystal with orientation \mathbf{g} . Eq. (3) is a conservation law which states that the rate of change of the volume fraction of crystals having orientations in a small element $d\mathbf{g}$ of the Euler space is equal to the net flux of crystal orientations into that element. The

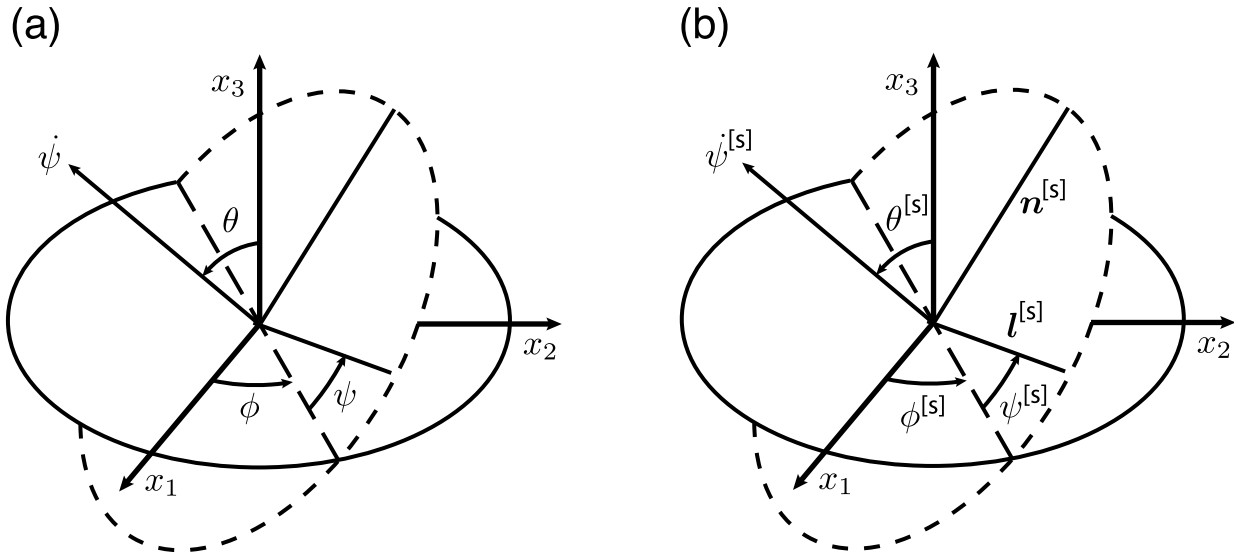


Figure 2. (a) General definition of the Eulerian angles (ϕ, θ, ψ) . (b) Definition of slip-system specific Eulerian angles $(\phi^{[s]}, \theta^{[s]}, \psi^{[s]})$ such that both the slip direction $l^{[s]}$ and the normal $n^{[s]}$ to the slip plane are in the plane perpendicular to the $\psi^{[s]}$ -axis.

spins $(\dot{\phi}, \dot{\theta}, \dot{\psi})$ are related to the Cartesian components ω_i of the spin by

$$\dot{\phi} = \omega_3 + (\omega_2 \cos \phi - \omega_1 \sin \phi) \cot \theta, \quad (4a)$$

$$\dot{\theta} = \omega_1 \cos \phi + \omega_2 \sin \phi, \quad (4b)$$

$$\dot{\psi} = (\omega_1 \sin \phi - \omega_2 \cos \phi) \csc \theta. \quad (4c)$$

Note also that the crystallographic spin ω is just the sum of the externally imposed rotation rate Ω and a contribution $\omega^{(c)}$ due to intracrystalline slip, or

$$\omega_i = \Omega_i - \epsilon_{ijk} l_j n_k \dot{\gamma} \equiv \Omega_i + \omega_i^{(c)}, \quad (5)$$

with ϵ_{ijk} the Levi-Civita symbol (component of the permutation tensor).

The spin $\dot{\mathbf{g}}$ is the fundamental quantity that will concern us in this study. It depends on the instantaneous macroscopic velocity gradient tensor \mathbf{D} , the components of which are

$$D_{ij} = E_{ij} - \epsilon_{ijk} \Omega_k, \quad (6)$$

where E_{ij} and Ω_k are the components of the SRT \mathbf{E} and the macroscopic rotation rate Ω of the polycrystal, respectively.

When the aggregate is deformed, each crystal within it responds by deforming in simple shear on planes normal to $\mathbf{n}(\mathbf{g})$ at a rate $\dot{\gamma}(\mathbf{g})$. The local velocity gradient tensor inside the crystal is thus

$$d_{ij} = \dot{\gamma} l_i n_j. \quad (7)$$

The local SRT e_{ij} is the symmetric part of d_{ij} , or

$$e_{ij} = \frac{\dot{\gamma}}{2} (l_i n_j + l_j n_i) \equiv \dot{\gamma} S_{ij}, \quad (8)$$

and Ω in eq. (5) is associated with the antisymmetric part of d_{ij} . Here S_{ij} is the Schmid tensor, which resolves the SRT inside each crystal onto the natural frame of reference of the slip system. It is symmetric and traceless and therefore has only five independent components. These can be expressed in terms of generalized spherical harmonics (GSH) T_l^{mn} of degree $l = 2$, where

$$T_l^{mn}(\phi, \theta, \psi) = e^{im\psi} P_l^{mn}(\cos \theta) e^{in\phi}, \quad (9)$$

and $P_l^{mn}(\cos \theta)$ is the associated Legendre polynomial (Bunge 1982, eq. 14.2). Explicit expressions for the independent components of the (slip-system specific) Schmid tensor $S_{ij}^{[s]}$ for the slip systems $s = 1, 2, 3$, are given in Appendix A.

Another kinematical object that plays an important role in our theory is the FSE associated with the deformation history experienced by a polycrystal. It is well known in fluid mechanics that an arbitrary time-dependent flow field transforms an initially spherical fluid element of infinitesimal size into an ellipsoid, called the FSE. The shape of the FSE can be characterized by the logarithms of the ratios of the lengths c_1, c_2 and c_3 of its axes, viz.

$$\begin{aligned} r_{12} &= \ln \frac{c_1}{c_2} \equiv (\mathcal{E}_{11} - \mathcal{E}_{22})t, & r_{23} &= \ln \frac{c_2}{c_3} \equiv (\mathcal{E}_{22} - \mathcal{E}_{33})t, \\ r_{31} &= \ln \frac{c_3}{c_1} \equiv (\mathcal{E}_{33} - \mathcal{E}_{11})t, \end{aligned} \quad (10)$$

where $\mathcal{E}_{11}, \mathcal{E}_{22}$ and \mathcal{E}_{33} are the principal strain-rates of the SRT \mathcal{E} that generates the background texture. Incompressibility of the fluid implies $r_{12} + r_{23} + r_{31} = 0$, so that only two of the quantities r_{ij} are independent. We also define an ‘equivalent strain’

$$r_0 = \frac{\sqrt{2}}{3} (r_{12}^2 + r_{23}^2 + r_{31}^2)^{1/2} = \frac{2}{3} (r_{12}^2 + r_{12}r_{23} + r_{23}^2)^{1/2}. \quad (11)$$

2.3 Slip-system rheology

Following standard practice, we assume that the slip rate $\dot{\gamma}^{[s]}$ on each slip system s obeys a power-law rheology of the form

$$\dot{\gamma}^{[s]} \propto \left| \frac{\tau}{\tau^{[s]}} \right|^{m^{[s]}-1} \frac{\tau}{\tau^{[s]}}, \quad (12)$$

where τ is the resolved shear stress (i.e. the shear stress acting on the slip plane in the slip direction), $\tau^{[s]}$ is a ‘critical resolved shear stress’ (CRSS) that measures the inherent resistance of the slip system to slip, and $m^{[s]}$ is a power-law exponent. Although the standard notation is to use n as the stress exponent, we have chosen m in this paper to avoid confusion with all the different occurrences of n . We assume $m^{[s]} = 3.5$ for all slip systems, following Bai *et al.* (1991). Because the macroscopic deformation rate of the aggregate is specified in our SO calculations, only the ratios

Table 1. Slip systems.

Index s	Slip plane	Slip direction	$\tau^{[s]}/\tau^{[2]}$	Exponent
1	(010)	[100]	0.25–4.0	3.5
2	(001)	[100]	1.0	3.5
3	(010)	[001]	0.25–4.0	3.5
4	(101)	$\bar{1}01$	100.0	3.5
5	(10 $\bar{1}$)	[101]	100.0	3.5

of the parameters $\tau^{[s]}$ (and not their absolute values) are relevant. In our calculations we assume $\tau^{[1]}/\tau^{[2]} \in [0.25, 4.0]$ and $\tau^{[2]}/\tau^{[3]} \in [0.25, 4.0]$ (see Table 1). Olivine deforming under upper mantle conditions is typically modelled with values of $\tau^{[1]}/\tau^{[2]} = 0.5$ and $\tau^{[2]}/\tau^{[3]} = 0.667$ (Kaminski *et al.* 2004) but this range of parameters also captures deformation under the low temperature low pressure ($\tau^{[1]}/\tau^{[2]} = 0.53$ and $\tau^{[2]}/\tau^{[3]} = 0.58$) and high-pressure high-temperature ($\tau^{[1]}/\tau^{[2]} = 0.73$ and $\tau^{[2]}/\tau^{[3]} = 0.39$) conditions considered by Castelnau *et al.* (2010). We note that these calculations also permit movement on the (100)[001], {021}[100] and {110}[001] slip systems, which are suppressed in our model. We characterize the CRSS ratios of the dominant slip systems $s = 1, 2$ and 3 in terms of the variables

$$p_{12} = \ln \frac{\tau^{[1]}}{\tau^{[2]}}, \quad p_{23} = \ln \frac{\tau^{[2]}}{\tau^{[3]}}. \quad (13)$$

Note also that

$$p_{31} = \ln \frac{\tau^{[3]}}{\tau^{[1]}} = -p_{12} - p_{23}. \quad (14)$$

In this study, we have assumed that the SO model requires each crystal in the aggregate to satisfy von Mises's criterion, according to which a crystal can only accommodate an arbitrary imposed deformation if it has at least five independent slip systems. However, it has recently been shown by Detrez *et al.* (2015) that the SO model requires each crystal in the aggregate deform by at least four independent slip systems, to ensure global strain compatibility. There are potential mechanisms which allow olivine to accommodate plastic deformation without satisfying the von Mises criterion. These include grain boundary sliding (e.g. Hirth & Kohlstedt 1995), diffusion (e.g. Chopra & Paterson 1984) and disclinations (e.g. Cordier 2014), but none of these mechanisms have been investigated in this study. To ensure numerical convergence of the SO model, we assume that each olivine crystal has, in addition to the three dominant slip systems mentioned previously, two harder systems, namely (101) $\bar{1}01$ and (10 $\bar{1}$)[101]. In our calculations we assume $\tau^{[4]}/\tau^{[2]} = \tau^{[5]}/\tau^{[2]} = 100$ (see Table 1). While these slip systems contribute significantly to the intracrystalline stress, they have a negligible (≈ 1 per cent) effect on the slip rates of the dominant systems. The model therefore gives valid predictions of the evolution of CPO.

3 ANALYTICAL PARAMETRIZATION

The considerations of the previous section imply that the instantaneous crystallographic rotation rate $\dot{\mathbf{g}}$ depends on the crystal's orientation \mathbf{g} ; the macroscopic SRT \mathbf{E} ; the already existing texture f ; and the parameters p_{12}, p_{23} and m that characterize the rheology of the slip systems:

$$\dot{\mathbf{g}} = \dot{\mathbf{g}}(\mathbf{g}, \mathbf{E}, f, p_{12}, p_{23}, m). \quad (15)$$

Here $\dot{\mathbf{g}}$ is understood as the slip-induced rotation rate, without the contribution due to the macroscopic vorticity which is the same for all crystals and can simply be added to $\dot{\mathbf{g}}$.

Next, we note that the spin components (4) take a particularly simple form when rewritten in terms of slip system-specific Eulerian angles ($\phi^{[s]}, \theta^{[s]}, \psi^{[s]}$) defined so that both the slip vector $\mathbf{l}^{[s]}$ and the vector $\mathbf{n}^{[s]}$ normal to the slip plane are perpendicular to the $\dot{\psi}^{[s]}$ -axis (Fig. 2b). The crystallographic spin $\dot{\mathbf{g}}^{[s]}$ produced by slip in the direction $\mathbf{l}^{[s]}$ on the plane $\mathbf{n}^{[s]}$ then has only a single non-zero component $\dot{\psi}^{[s]}$, and $\dot{\phi}^{[s]} = \dot{\theta}^{[s]} = 0$ identically. Fig. 2(b) implies that $l_i^{[1]} = a_{1i}$ and $n_i^{[1]} = a_{2i}$, where a_{ij} are given by (1) with $(\phi, \theta, \psi) \rightarrow (\phi^{[s]}, \theta^{[s]}, \psi^{[s]})$. Ignoring the macroscopic vorticity as explained above, we find that eqs (4) and (5) simplify to

$$\dot{\phi}^{[s]} = \dot{\theta}^{[s]} = 0, \quad \dot{\psi}^{[s]} = -\dot{\gamma}^{[s]}(\mathbf{g}^{[s]}). \quad (16)$$

Thus, the crystallographic spin due to slip is simply the negative of the shear rate on the slip system in question.

To go further, we first note the obvious difficulty that the space of possible background textures f is infinite. To make progress, therefore, we need to restrict and parameterize this space in some way. Our choice is to consider the space of all textures produced by uniform triaxial straining of an initially isotropic aggregate, which can be parameterized by the axial ratios r_{12} and r_{23} of the associated FSE. Accordingly, the functional dependence we need to determine becomes

$$\dot{\gamma}^{[s]} = \dot{\gamma}^{[s]}(\mathbf{g}^{[s]}, \mathbf{E}, r_{12}, r_{23}, p_{12}, p_{23}, m). \quad (17)$$

This still seems impossibly complex, so we now call the SO model to our aid. Consider the case of uniaxial compression along the x_3 -axis at a rate $\dot{\epsilon}$, for which the nonzero components of the SRT are $E_{33} = -\dot{\epsilon}$, $E_{11} = E_{22} = \dot{\epsilon}/2$. The shear rate $\dot{\gamma}^{[1]}$ and the ODF f are then independent of the Eulerian angle $\phi^{[1]}$ by symmetry. Fig. 3 shows the spin $\dot{\psi}^{[1]}(\theta^{[1]}, \psi^{[1]})$ for the slip system (010)[100] ($s = 1$) predicted by the SO model with $p_{12} = p_{23} = 0$ ($\tau^{[1]} = \tau^{[2]} = \tau^{[3]}$) at two different equivalent strains $r_0 \equiv |\dot{\epsilon}_3|t = 0$ (Fig. 3a) and $r_0 = 0.4$ (Fig. 3b). Remarkably, the images of Figs. 3(a) and (b) appear to be the same function with different amplitudes. A more detailed investigation shows that this impression is correct, and that the function in question is $F = b \sin 2\psi^{[1]} \sin^2 \theta^{[1]}$, where b is an unknown amplitude. Least-squares fitting of this expression to the numerical predictions yields $b = 1.25$ for Fig. 3(a) and $b = 1.71$ for Fig. 3(b), with a nearly perfect fit (variance reduction = 99.9 per cent) in both cases.

Next, we note that the function $\sin 2\psi^{[1]} \sin^2 \theta^{[1]}$ can be written as

$$\sin 2\psi^{[1]} \sin^2 \theta^{[1]} = -\frac{2\sqrt{3}}{3} T_2'^{20} = -2 \left(S_{11}^{[1]} + S_{22}^{[1]} \right), \quad (18)$$

where $T_2'^{20}$ is a GSH, defined as $T_l'^{mn} = 2^{-1/2} i^{1+m-n} (T_l^{mn} - T_l^{-m-n})$ (Bunge 1982, eq. 14.37), where $i = \sqrt{-1}$. This result has two surprising and far-reaching implications. First, the angular dependence of the spin ($\propto \sin 2\psi^{[1]} \sin^2 \theta^{[1]}$ in this case) remains the same regardless of the strength of the background texture; it is only the amplitude of the function that depends on the texture. Second, it suggests that the angular dependence of the spin is always a GSH of degree $l = 2$, without any contribution from higher-degree harmonics. Noting further that the shear rate $\dot{\gamma}^{[s]}$ must depend linearly on the imposed macroscopic strain rate \mathbf{E} , we are led to propose the following expression for $\dot{\gamma}^{[s]}$:

$$\dot{\gamma}^{[s]} = -\dot{\psi}^{[s]} = A_{ijkl}^{[s]}(r_{12}, r_{23}, p_{12}, p_{23}, m) S_{ij}^{[s]} E_{kl}, \quad (19)$$

where \mathbf{A} is a fourth-order 'spin tensor'. The superscripts $[s]$ denote the index of the slip system ($s = 1, 2$ or 3). In the next section we determine how the spin tensor A_{ijkl} depends on its five arguments.

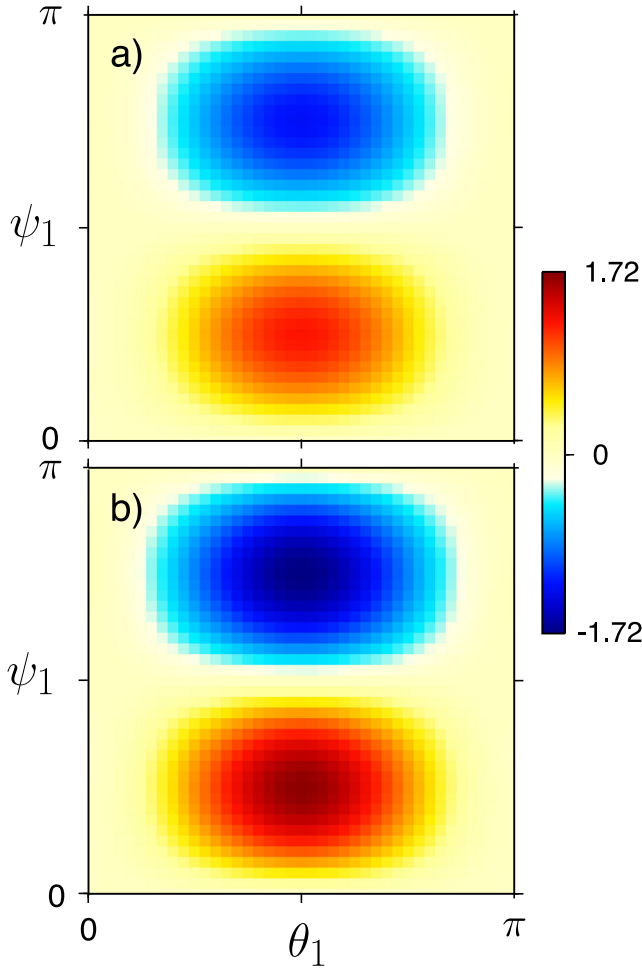


Figure 3. Instantaneous crystallographic spin $\psi^{[1]}(\theta^{[1]}, \psi^{[1]})$ for the slip system (010)[100], predicted by the SO model with $\tau^{[1]}/\tau^{[2]} = \tau^{[2]}/\tau^{[3]} = 1$ for an initially isotropic olivine aggregate deformed in uniaxial compression. (a) $|\dot{\epsilon}_3|t = 0$; (b) $|\dot{\epsilon}_3|t = 0.4$. Colour scale is in units of the axial shortening rate $\dot{\epsilon}_3 < 0$. The Eulerian angles $\theta^{[1]}$ and $\psi^{[1]}$ are defined as in Fig. 2(b).

4 PARAMETRIZATION OF THE SPIN TENSOR A

4.1 SO model calculations

We now use the SO model as a benchmark to determine the tensor components $A_{ijkl}(r_{12}, r_{23}, p_{12}, p_{23}, m)$. The procedure comprises two steps: (1) generation of the background texture and (2) calculation of the instantaneous spin induced by applying a given rate of strain to the background texture. Thus in step (1), we first select the number of crystals N in the model aggregate ($= 2000$ in all cases) and the values of the slip-system parameters p_{12} , p_{23} , and m ($= 3.5$ in all cases). We also choose the components of the SRT \mathcal{E} that generates the background texture. We work in the reference frame of the FSE, which means that

$$\mathcal{E} = \begin{pmatrix} \mathcal{E}_{11} & 0 & 0 \\ 0 & \mathcal{E}_{22} & 0 \\ 0 & 0 & \mathcal{E}_{33} \end{pmatrix}. \quad (20)$$

This limits the model to orthotropic CPO, which is sound for practical purposes as natural CPO most often exhibit such a symmetry. The SO model is then run starting from an isotropic initial condition

until target values of the FSE axial ratios r_{12} and r_{23} are reached. In step 2, we apply an instantaneous SRT

$$\mathbf{E} = \begin{pmatrix} E_{11} & E_{12} & E_{13} \\ E_{12} & E_{22} & E_{23} \\ E_{13} & E_{23} & E_{33} \end{pmatrix} \quad (21)$$

to the background texture. Note that \mathbf{E} need not be the same as \mathcal{E} , which allows us to obtain results for arbitrary orientations of the principal axes of \mathbf{E} relative to those of \mathcal{E} .

The final result of the procedure described above is a set of slip rates $\dot{\gamma}_n^{[s]}$ on each of the three slip systems ($s = 1, 2$ or 3 in Table 1) and for each of the n phases ($n = 1, 2, \dots, N$). The calculated values of $\dot{\gamma}_n^{[s]}$ are then substituted into eq. (5) to obtain the ‘partial’ spins $\omega_i^{[s]}$ due to the actions of the individual slip systems, and which are related to the total spin ω_i by

$$\omega_i = \sum_{s=1}^3 \omega_i^{[s]}. \quad (22)$$

Finally, by substituting the partial spins $\omega_i^{[s]}$ into eq. (4) and expressing the results in terms of the slip system-specific Eulerian angles $(\phi^{[s]}, \theta^{[s]}, \psi^{[s]}) \equiv \mathbf{g}^{[s]}$, we obtain the rotation rates $\dot{\psi}_n^{[s]}$ for all grains n and slip systems s .

4.2 ANPAR model for crystallographic spin

At this point, we have a large library of numerical solutions, but little idea of what they imply about the structure of the function $A_{ijkl}^{[s]}(r_{12}, r_{23}, p_{12}, p_{23}, m)$. As a first simplification, we assume that the dependence on r_{12} and r_{23} is separable from the dependence on p_{12} and p_{23} , that is,

$$A_{ijkl}^{[s]} = H^{[s]}(p_{12}, p_{23}, m) Q_{ijkl}(r_{12}, r_{23}). \quad (23)$$

The first factor $H^{[s]}$ in eq. (23) describes how the activities of the three slip systems depend on the CRSS ratios at the initial instant ($r_{12} = r_{23} = 0$) of the deformation, while the factor $Q_{ijkl}(r_{12}, r_{23})$ describes how the activities of slip systems with equal strengths ($p_{12} = p_{23} = 0$) vary as a function of strain for arbitrary deformations.

Consider first the factor $Q_{ijkl}(r_{12}, r_{23})$. Since E_{ij} and $S_{ij}^{[s]}$ are both symmetric and traceless, there are at most 25 independent products of them, or equivalently 25 independent Q_{ijkl} . However, we have found that $Q_{ijkl}(r_{12}, r_{23})$ obeys surprising symmetries that reduce the number of its independent non-zero components to just two. We began by fixing $H^{[s]}(0, 0, 3.5) = 1$ and performing a least-squares fit of the model (19) to the spin predicted by the SO model. We did this for 217 different values of (r_{12}, r_{23}) , where both r_{12} and r_{23} were in the range $[-0.9, 0.9]$, which is within the range of finite strain that can be successfully modelled by the SO approach. The sampled points were equally spaced along radial lines in the (r_{12}, r_{23}) -plane. For each of the sampled points we repeated the fit for five random instantaneous SRTs, giving a total of 1085 fits of our model to the numerical solutions of the SO model. This allowed us to discover numerically that 18 of the coefficients Q_{ijkl} were identically zero. We also found at this stage that $Q_{1122} \approx Q_{2211}$. These two numerical results implied that the tensor Q_{ijkl} exhibits *major* symmetry, that is, $Q_{ijkl} = Q_{klij}$. This leaves only six independent, non-zero components of Q_{ijkl} , namely Q_{1111} , Q_{1122} , Q_{2222} , Q_{1212} , Q_{1313} and Q_{2323} .

Relationships among the six remaining non-zero Q_{ijkl} arise from the fact that the labelling of the coordinate axes is arbitrary. We can have a cyclic permutation of the coordinate axes from (1, 2, 3) to

(2, 3, 1) or (3, 1, 2), or a non-cyclic permutation from (1, 2, 3) to (1, 3, 2), (2, 1, 3) or (3, 2, 1). The spin $\dot{\psi}^{[s]}$ has to be invariant under a relabelling of the coordinate axes. Equating the expressions for $\dot{\psi}^{[s]}$ in the original and the transformed coordinate systems allows us to derive rigorous transformation rules (in the reference frame of the FSE). Setting $B = Q_{1111}$ and $C = Q_{1212}$, we find that

$$Q_{1212}(r_{12}, r_{23}) = C(r_{12}, r_{23}), \quad (24a)$$

$$Q_{1313}(r_{12}, r_{23}) = C(r_{31}, r_{23}), \quad (24b)$$

$$Q_{2323}(r_{12}, r_{23}) = C(r_{23}, r_{12}), \quad (24c)$$

$$Q_{1111}(r_{12}, r_{23}) = B(r_{12}, r_{23}), \quad (24d)$$

$$Q_{2222}(r_{12}, r_{23}) = B(r_{12}, r_{31}), \quad (24e)$$

$$Q_{1122}(r_{12}, r_{23}) = \frac{1}{2} [B(r_{23}, r_{12}) - B(r_{12}, r_{23}) - B(r_{12}, r_{31})]. \quad (24f)$$

These symmetries reduce the number of independent coefficients Q_{ijkl} to just two, which we take to be Q_{1111} and Q_{1212} .

Now consider the factor $H^{[s]}$ in eq. (23). We have discovered numerically that $H^{[2]}$ and $H^{[3]}$ can be obtained from $H^{[1]}$ by simple variable transformations:

$$\begin{aligned} H^{[2]}(p_{12}, p_{23}) &= H^{[1]}(-p_{12}, -p_{31}), \\ H^{[3]}(p_{12}, p_{23}) &= H^{[1]}(-p_{23}, -p_{12}). \end{aligned} \quad (25)$$

Combining this with the previous results for Q_{ijkl} , we obtain the following general ANPAR model for the crystallographic spin, which is valid on each slip system s :

$$\begin{aligned} \dot{\psi}^{[s]} &= \frac{1}{2} H^{[s]}(p_{12}, p_{23}) \\ &\times \left\{ B(r_{12}, r_{23}) [(-4E_{11} + E_{22}) S_{11}^{[s]} + (E_{11} + 2E_{22}) S_{22}^{[s]}] \right. \\ &- B(r_{23}, r_{12}) [(4E_{11} + 5E_{22}) S_{11}^{[s]} + (5E_{11} + 4E_{22}) S_{22}^{[s]}] \\ &+ B(r_{12}, r_{31}) [(2E_{11} + E_{22}) S_{11}^{[s]} + (E_{11} - 4E_{22}) S_{22}^{[s]}] \\ &- 8[C(r_{12}, r_{23}) E_{12} S_{12}^{[s]} + C(r_{23}, r_{12}) E_{23} S_{23}^{[s]}] \\ &\left. + C(r_{31}, r_{23}) E_{31} S_{31}^{[s]} \right\}. \end{aligned} \quad (26)$$

Note that the coefficient C multiplies the off-diagonal components of \mathbf{E} , and is therefore not needed for coaxial deformations where the principal axes of the SRT and the FSE are aligned.

The final part of the ANPAR procedure is to calculate the total spin for each crystal. Substituting the above slip-specific spin (26) into eq. (16) provides us with the slip rates $\dot{\gamma}^{[s]}$ on each of the three slip systems ($s = 1, 2$ or 3 in Table 1). The calculated values of $\dot{\gamma}^{[s]}$ are then substituted into eq. (5) to obtain the Cartesian components of the spin $\omega_i^{[s]}$ due to the actions of the individual slip systems, and which are related to the total spin ω_i by eq. (22). Finally, by substituting ω_i into eq. (4) we obtain the total spin $(\dot{\phi}, \dot{\theta}, \dot{\psi}) \equiv \dot{\mathbf{g}}$ of an individual crystal, in terms of the Eulerian angles.

4.3 Numerical determination of the parametrization coefficients

The symmetries outlined above indicate that we only require analytical expressions for the three functions B , C and $H^{[1]}$. Full details

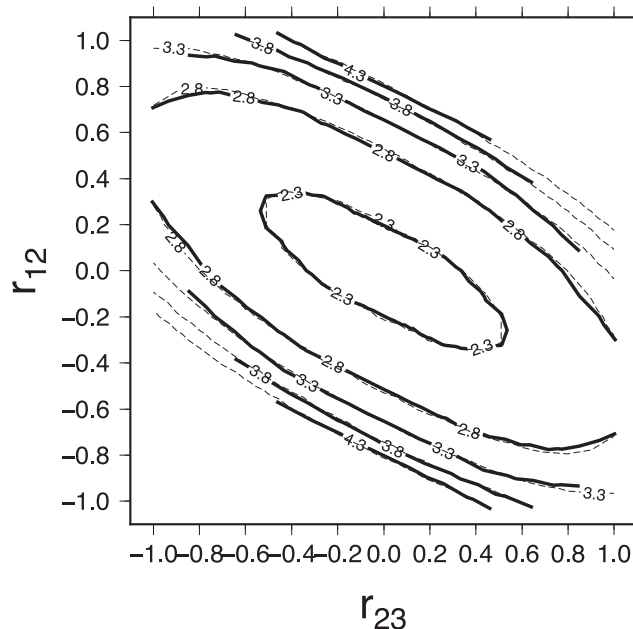


Figure 4. Spin amplitude B as a function of deformation when the strengths of the dominant slip systems are all equal, shown as a function of the axial ratios of the finite strain ellipsoid. Solid contours show the amplitude B that best fits the predictions of the SO model, and the dashed contours show the fitting function (B3).

of the expressions obtained and the methods used are given in Appendix B. Briefly, we first obtain models for B and C , by setting equal slip-system strengths ($p_{12} = p_{23} = 0$) and fixing $H^{[1]}(0, 0) = 1$ in eq. (26). We then capture B and C data by a least-squares fit of the model (26) to the spin predicted by the SO model, for sampled values of r_{12} and r_{23} , and random instantaneous SRTs. In each case, the variance reduction of the fit $R \geq 99.7$ per cent. Simple polynomials in r_{12} and r_{23} are fitted to the B and C data (using least squares) to obtain the analytical expressions (B3). The root mean square (RMS) errors of the fits are 0.039 and 0.0070, respectively. Figs 4 and 5 display contour plots of the models (B3) against the B and C data, respectively.

To obtain an analytical expression for $H^{[1]}$, we capture $H^{[1]}$ data over the entire admissible range of (p_{12}, p_{23}) values for olivine. Using eq. (13) and the CRSS ratios assumed in Table 1, this gives admissible values of p_{12} and p_{23} in the range $[-\ln 4, \ln 4] = [-1.386, 1.386]$. We fit eq. (26) to 81 instantaneous ($t = 0$, i.e. isotropic CPO) numerical solutions of the SO model for uniaxial compression, with equally spaced points in the (p_{12}, p_{23}) -plane with p_{12} and p_{23} in the above admissible range. Simple polynomials in p_{12} and p_{23} are fitted to the $H^{[1]}$ data using least squares, leading to the analytical expression (B6). The RMS error of the fit is 0.0068.

Finally, we test the assumption (23) that A_{ijkl} can be written as a product of a scalar $H^{[s]}$ (that depends on p_{12} and p_{23}) and a tensor Q_{ijkl} (that depends on r_{12} and r_{23}). We substituted the analytical expressions for B , C and $H^{[1]}$ (see eqs B3 and B6, respectively) into the full model for the spin on each slip system (26). We then fitted these models to the spin predicted by the SO model for random background textures (formed from various r_{12} , r_{23} , p_{12} and p_{23} values) and random instantaneous SRTs. Remarkably, in each case, the variance reduction $R > 99.1$ per cent and in most cases $R > 99.7$ per cent.

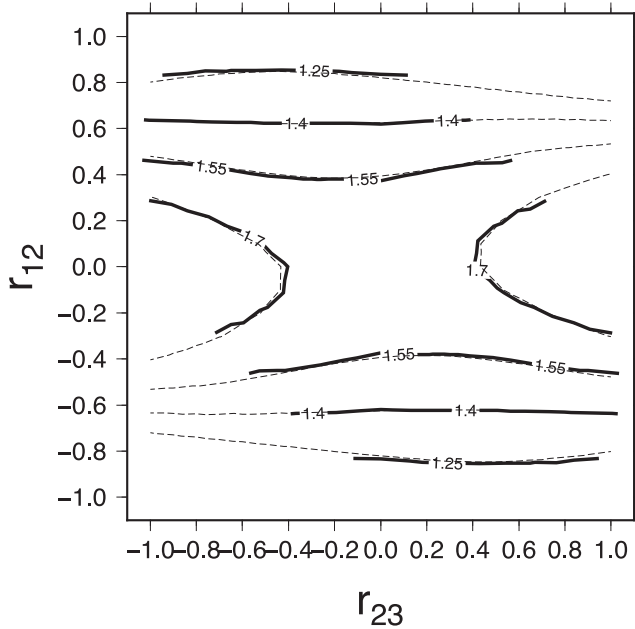


Figure 5. Same as Fig. 4, but for the spin amplitude C .

5 EVOLUTION OF CPO DURING PROGRESSIVE DEFORMATION

The results in the previous sections imply that the ANPAR model provides an accurate and efficient substitute for the much more computationally expensive SO model. We now demonstrate this in more detail by comparing the textures predicted by the two models for olivine polycrystals subjected to various kinds of finite deformation. In the following three test cases (for uniform deformation) the strain increment used ($\Delta r_0 = 0.025$) is the same for both the SO and ANPAR models. The different components of our method for ANPAR CPO calculation are summarized in Algorithm 1.

5.1 Irrotational deformations

Our first test case is a uniaxial compression to a strain $r_{23} = 0.9$, $r_{12} = 0$, with CRSS ratios $\tau^{[1]}/\tau^{[2]} = 0.5$ and $\tau^{[2]}/\tau^{[3]} = 0.667$. Fig. 6 shows the (100), (010) and (001) pole figures predicted for this case by the SO model (Fig. 6a) and the ANPAR model (Fig. 6b). The two sets of pole figures are practically indistinguishable (variance reduction $R > 99.9$ per cent. Variance reduction for pole figures is defined in Appendix C). However, the ANPAR

model is a remarkable 1.75×10^4 times quicker than the SO model (0.0344 s for ANPAR versus 603 s for SO).

To quantify the agreement in another way, we used the obtained CPO to calculate the effective elastic behaviour of the aggregate for the SO and ANPAR models using the MSAT software (Walker & Wookey 2012). An element-by-element comparison of the two Voigt–Reuss–Hill average elastic stiffness tensors gives a maximum absolute difference of 0.19 GPa between SO and ANPAR, which is not significant for geophysical purposes.

As a second test, Fig. 7 shows the predicted pole figures for uniform deformation by pure shear in the x_1 – x_3 plane to a strain $r_{12} = r_{23} = 0.563$, again with CRSS ratios $\tau^{[1]}/\tau^{[2]} = 0.5$ and $\tau^{[2]}/\tau^{[3]} = 0.667$. Again, the two sets of pole figures and the predicted elasticity are nearly identical (variance reduction 99.3 per cent, maximum absolute difference in the predicted elasticity 0.16 GPa). In this case, the speed of the ANPAR model is 3.1×10^4 greater than that of the SO model (0.0348 s for ANPAR versus 1090 s for SO).

5.2 Rotational deformations

Rotational deformations are those in which the axes of the FSE do not remain aligned with the principal axes of the SRT as the deformation progresses.

As an example, consider the case of simple shear, for which the major axis of the FSE is initially aligned with the SRT but then rotates progressively away from it towards the shear plane. As a result, both functions B and C in eq. (26) come into play.

Let $\dot{\epsilon}_1$ be the maximum rate of extension along the x_1 axis. The elongation of the FSE at time t can then be described by the axial ratio $\mathcal{R} = \exp(r_{12}) = \exp(2 \sinh^{-1}[\dot{\epsilon}_1 t])$ (Ribe & Yu 1991, eq. 16). If we denote $\chi(t)$ the angle between the two frames, then $\chi(0) = 0$ and $\lim_{t \rightarrow \infty} \chi(t) = -\pi/4$. Using the standard tensor transformation rule, we obtain a velocity gradient tensor of the form $\mathbf{D} = \mathbf{E} + \mathbf{W}$, where

$$\mathbf{E} = \dot{\epsilon}_1 \begin{pmatrix} \cos 2\chi & \sin 2\chi & 0 \\ \sin 2\chi & -\cos 2\chi & 0 \\ 0 & 0 & 0 \end{pmatrix}, \quad \mathbf{W} = \dot{\epsilon}_1 \begin{pmatrix} 0 & -1 & 0 \\ 1 & 0 & 0 \\ 0 & 0 & 0 \end{pmatrix} \quad (27)$$

are the respective strain-rate and rotation-rate, tensors and $\chi = -\frac{1}{2} \tan^{-1}(\dot{\epsilon}_1 t)$. We used CRSS ratios $\tau^{[1]}/\tau^{[2]} = 0.5$ and $\tau^{[2]}/\tau^{[3]} = 0.667$. We updated the velocity gradient tensor at each time step to remain in the frame of reference of the FSE.

Algorithm 1. ANPAR CPO calculations for Olivine.

- | | |
|--|---|
| (1) Set N | (Number of grains ($n = 1, \dots, N$)) |
| (2) Set initial isotropic texture $\mathbf{g}_n[0] = (\phi_n[0], \theta_n[0], \psi_n[0])$. | |
| (3) Set p_{12}, p_{23} | (CRSS ratios) |
| (4) Set $r_{12}[0] = r_{23}[0] = 0$. | (FSE initially a sphere) |
| (5) For $k = 1, \dots, K$ do | (Calculate texture at each time-step) |
| (i) Set $\mathbf{E}[k]$ and $\mathbf{\Omega}[k]$ | (SRT and macroscopic rotation rate) |
| (ii) Transform SRT into reference frame of FSE | |
| (iii) Calculate $\mathbf{D}[k]$ | (velocity gradient tensor, using eq. 6) |
| (iv) Set $r_0[k]$ | (strain increment) |
| (v) Calculate $r_{12}[k], r_{23}[k]$ and t_k | (FSE parameters and time-step, using eqs 10 and 11) |
| (vi) Calculate slip-rates $\dot{\gamma}_n^{[s]}[k]$ | (using eqs 16 and 26) |
| (vii) Calculate rotation rates $\dot{\mathbf{g}}_n[k] = (\dot{\phi}_n[k], \dot{\theta}_n[k], \dot{\psi}_n[k])$ | (using eqs 4 and 5) |
| (viii) Update texture $\mathbf{g}_n[k] = (\phi_n[k], \theta_n[k], \psi_n[k])$ | (integrating forward in time) |
| end do | |
| (6) Plot texture $\mathbf{g}_n[K] = (\phi_n[K], \theta_n[K], \psi_n[K])$ | (using MTEX) |

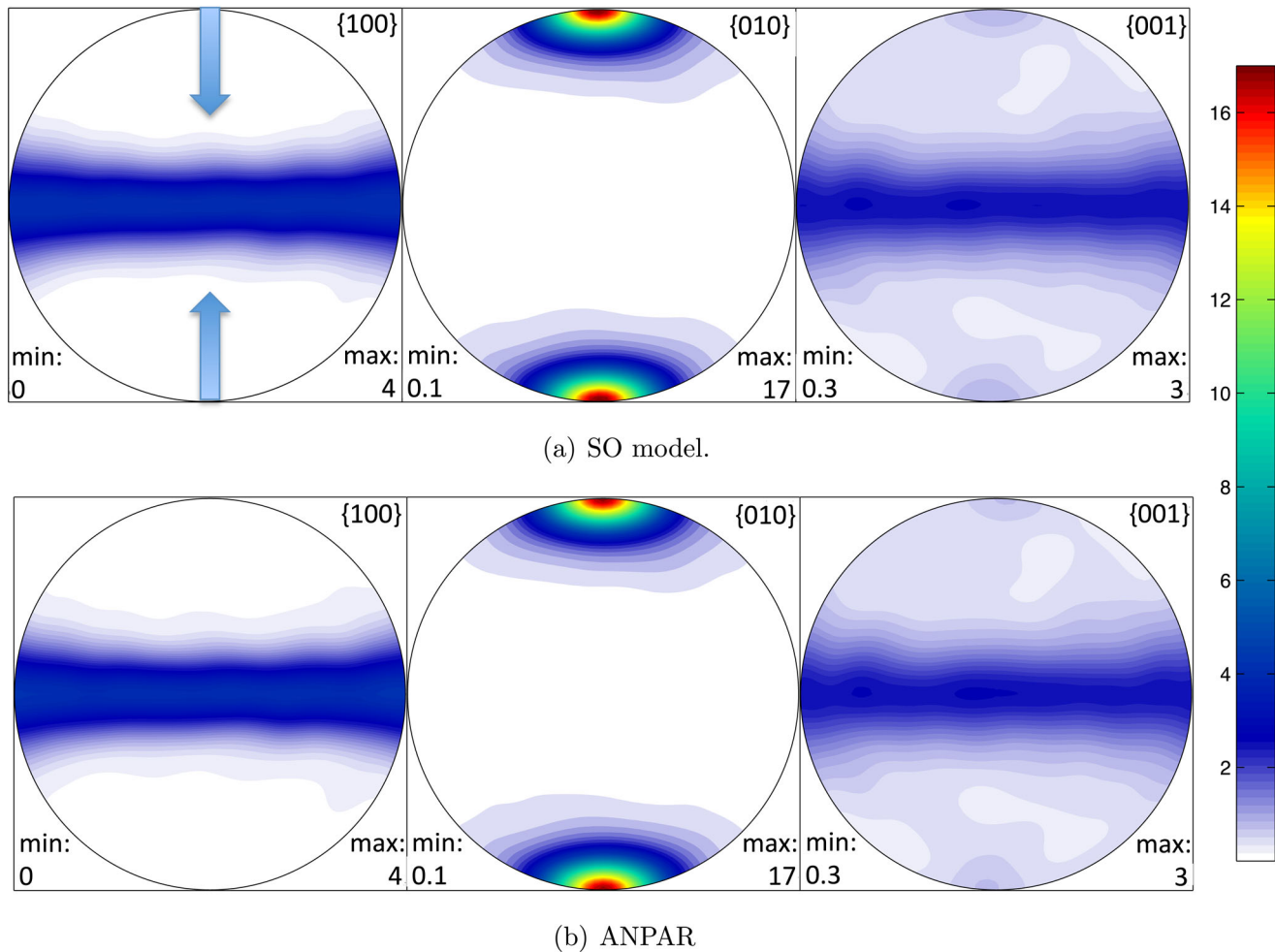


Figure 6. Pole figures (equal-area projections) for an olivine polycrystal deformed by uniaxial compression to a strain $r_{23} = 0.9$, $r_{12} = 0$. The arrows indicate the compression (x_3 -) axis, which extends from the bottom to the top of each figure. The predictions of (a) the SO model and (b) the analytical model (ANPAR) are shown for critical resolved shear stress ratios $\tau^{[1]}/\tau^{[2]} = 0.5$ and $\tau^{[2]}/\tau^{[3]} = 0.667$. Figure generated using MTEX (Bachmann *et al.* 2010).

Fig. 8 shows the pole figures predicted by our theory together with those predicted by the SO model for $\dot{\epsilon}_1 = 1$ and $r_0 = 0.5$. Yet again, the two sets of pole figures are nearly indistinguishable, with a variance reduction $R = 99.5$ per cent and a maximum difference in the predicted elasticity of 0.77 GPa. The speed of the ANPAR model is 5.6×10^4 greater than that of the SO model (0.367 s for ANPAR versus 2062 s for SO).

5.3 Non-Newtonian corner-flow model for a spreading ridge

Our final example is a more complex and non-uniform geophysical flow, namely the flow in the mantle beneath an ocean ridge. This flow can be simply modeled using the ‘corner flow’ similarity solution of the Stokes equation in polar coordinates (r, φ) (Batchelor 1967). Fig. 9 shows the geometry and boundary conditions appropriate for a ridge crest (Lachenbruch & Nathenson 1974). Flow in the asthenosphere $0 < \varphi < \alpha$ is driven by the horizontal motion of wedge-shaped surface plates at velocity U_0 . The solid lines with arrows show typical streamlines of the flow for an asthenosphere with a power law rheology with power law index $n = 3$ (Tovish *et al.* 1978). The two streamlines are for $\varphi_0 = 10^\circ$ and 20° , and we use $\alpha = 60^\circ$ throughout this subsection.

The steady incompressible Stokes equations and the boundary conditions in Fig. 9 can be satisfied if the stream function Ψ has the self-similar form

$$\Psi = U_0 r F(\varphi), \quad (28)$$

which is valid for both Newtonian ($n = 1$) and non-Newtonian ($n \neq 1$) fluids. Here we use $n = 3$, corresponding to a rheology that is close to that of olivine at high stresses ($n \approx 3.5$; Bai *et al.* 1991). The function $F(\varphi)$ for $n = 3$ is of the form

$$F(\varphi) = A \sin \varphi + Ch(\varphi, D), \quad (29)$$

where

$$h(\varphi, D) = 27 \cos \left[\frac{\sqrt{5}}{3}(\varphi + D) \right] - \cos \left[\sqrt{5}(\varphi + D) \right]. \quad (30)$$

The constants A , C and D are chosen to satisfy the boundary conditions, yielding

$$D = \frac{3\pi}{2\sqrt{5}}, \quad (31)$$

$$C = -[h(\alpha, D) \cos \alpha - h_\varphi(\alpha, D) \sin \alpha]^{-1}, \quad (32)$$

$$A = -C [h(\alpha, D) \sin \alpha + h_\varphi(\alpha, D) \cos \alpha], \quad (33)$$

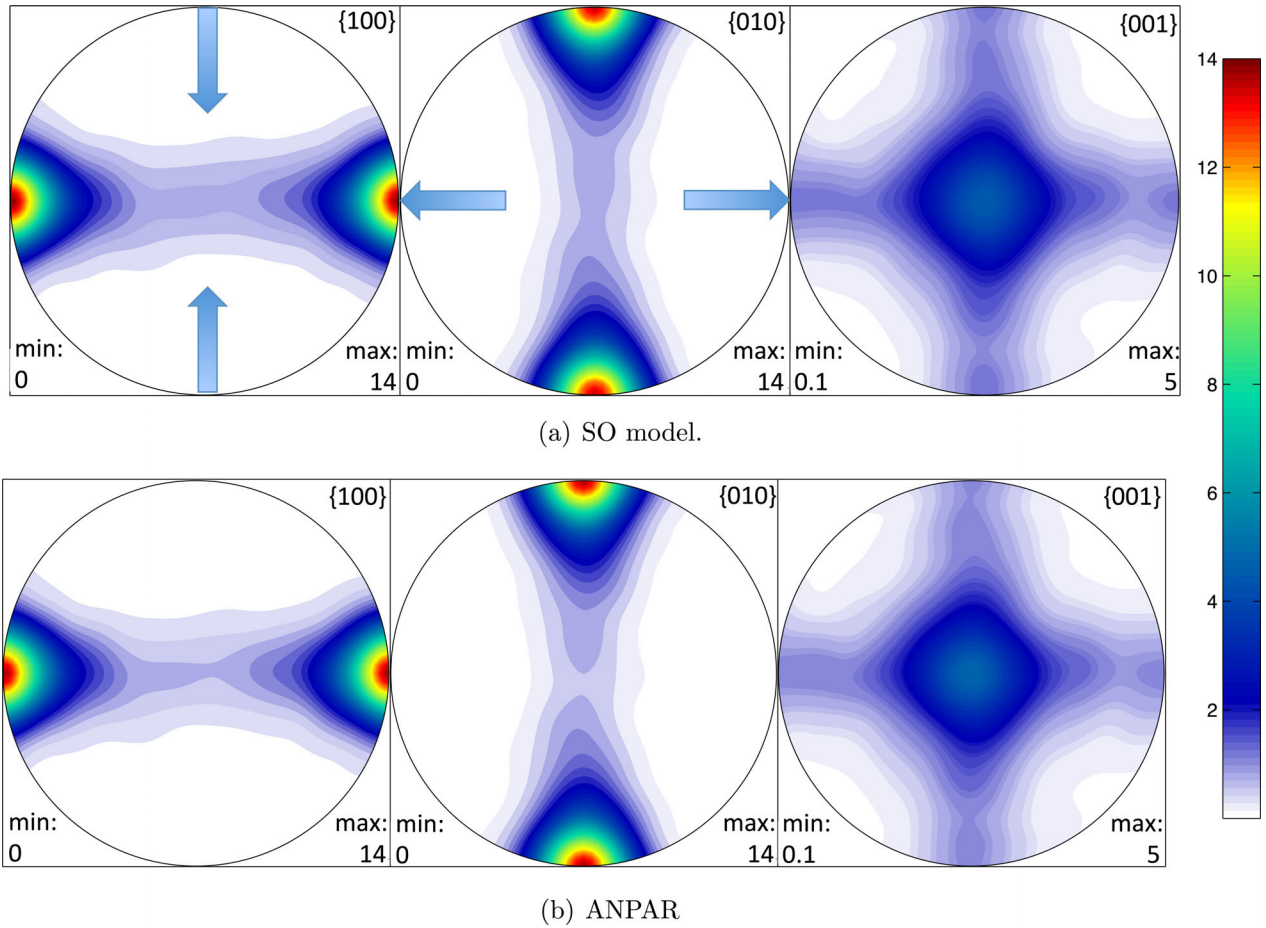


Figure 7. Same as Fig. 6, but for deformation by pure shear to $r_{12} = r_{23} = 0.563$. The axes of maximum extension (x_1) and compression (x_3) are indicated by the arrows.

where $h_\varphi = dh/d\varphi$. The maximum strain rate $\dot{\epsilon}$ is

$$\dot{\epsilon} = U_0 \frac{|F'' + F|}{2r}, \quad (34)$$

where $F'' = \frac{d^2}{d\varphi^2} F(\varphi)$, and the local rotation rate (= one-half the vorticity) is

$$\Omega = -U_0 \frac{F'' + F}{2r}. \quad (35)$$

To proceed, we require knowledge of the FSE as we progress along a streamline. We obtain the axial ratio $\mathcal{R} = \exp(r_{12})$ of the FSE and the orientation χ of the FSE by solving the following evolution equations (Kellogg & Turcotte 1990; Ribe 1992):

$$\dot{\mathcal{R}} = 2\mathcal{R} (E_{11} \cos 2\chi + E_{12} \sin 2\chi), \quad (36)$$

$$\dot{\chi} = \Omega + \frac{1 + \mathcal{R}^2}{1 - \mathcal{R}^2} (E_{11} \sin 2\chi - E_{12} \cos 2\chi). \quad (37)$$

The above equations can be simplified by transforming the Cartesian strain rate components E_{ij} to polar coordinates, and then expressing the time derivatives in terms of a φ -derivative (McKenzie 1979, eq. 6):

$$\frac{D}{Dt} = -\frac{U_0 F}{r} \frac{d}{d\varphi}, \quad (38)$$

This leads to the following simplified form for the evolution equations:

$$\frac{d\mathcal{R}}{d\varphi} = -\mathcal{R} \frac{F'' + F}{F} \sin 2(\chi - \varphi), \quad (39)$$

$$\frac{d\chi}{d\varphi} = \frac{F'' + F}{2F} \left[1 + \frac{1 + \mathcal{R}^2}{1 - \mathcal{R}^2} \cos 2(\chi - \varphi) \right] \quad (40)$$

which must be solved subject to the following initial conditions at $\varphi = \varphi_0$:

$$\mathcal{R}(\varphi_0) = 1, \quad (41)$$

$$\chi(\varphi_0) = \varphi_0 + \frac{\pi}{4}. \quad (42)$$

These evolution equations were solved using a fourth-order Runge–Kutta method. In Fig. 9, the FSE is plotted at different points along two different streamlines.

In polar coordinates the velocity gradient tensor is of the form (McKenzie 1979)

$$\mathbf{D} = \begin{pmatrix} 0 & -2\Omega & 0 \\ 0 & 0 & 0 \\ 0 & 0 & 0 \end{pmatrix}, \quad (43)$$

where Ω is given by eq. (35). However, to calculate CPO, we have to transform back into Cartesian coordinates. In doing this, we obtain

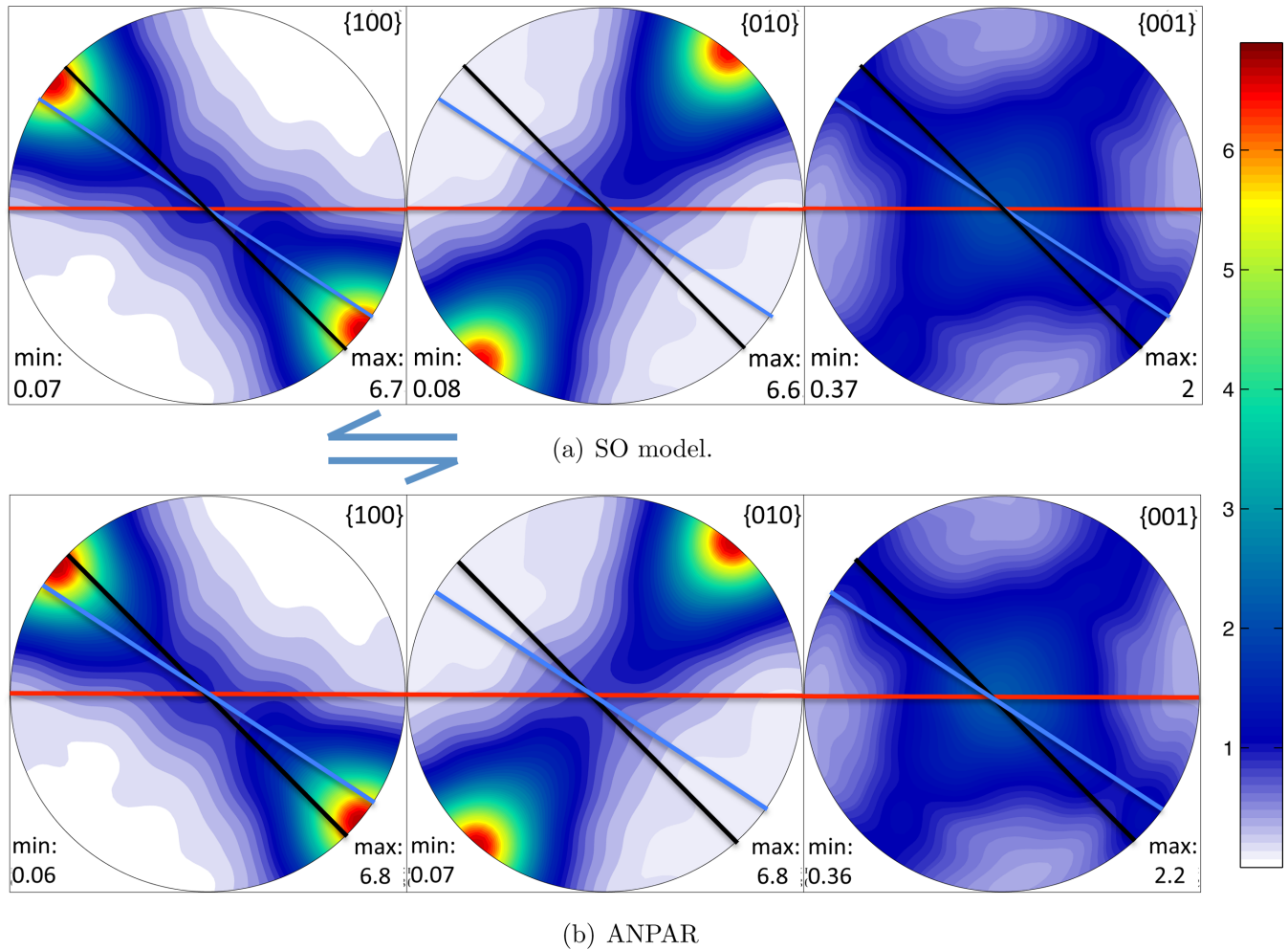


Figure 8. Same as Fig. 6, but for deformation by simple shear to $r_{12} = 0.841$, $r_{23} = -0.421$ ($r_0 = 0.5$), with CRSS ratios $\tau^{[1]}/\tau^{[2]} = 0.5$ and $\tau^{[2]}/\tau^{[3]} = 0.667$. The black, red and blue lines indicate the axis of maximum instantaneous extension (x_1), the shear plane and the long axis of the FSE, respectively. The direction of shear is indicated.

a velocity gradient tensor of the form $\mathbf{D} = \mathbf{E} + \mathbf{W}$, where

$$\mathbf{E} = \dot{\epsilon} \begin{pmatrix} -\sin 2\varphi & \cos 2\varphi & 0 \\ \cos 2\varphi & \sin 2\varphi & 0 \\ 0 & 0 & 0 \end{pmatrix}, \quad \mathbf{W} = \dot{\epsilon} \begin{pmatrix} 0 & 1 & 0 \\ -1 & 0 & 0 \\ 0 & 0 & 0 \end{pmatrix}. \quad (44)$$

We then use the standard tensor transformation rule to transform the SRT into the reference frame of the FSE. This gives

$$\mathbf{E} = \dot{\epsilon} \begin{pmatrix} \sin 2(\chi - \varphi) & \cos 2(\chi - \varphi) & 0 \\ \cos 2(\chi - \varphi) & -\sin 2(\chi - \varphi) & 0 \\ 0 & 0 & 0 \end{pmatrix}. \quad (45)$$

Fig. 10 shows the pole figures predicted by our theory together with those predicted by the SO model for an equivalent strain with those predicted by the SO model for an equivalent strain $r_0 = 0.6$ ($r_{12} = 1.047$, $r_{23} = -0.523$). This was for the first streamline $\varphi_0 = 10^\circ$ in Fig. 10, with $\varphi = 49^\circ$ and $\chi = 67^\circ$. Again, the two sets of pole figures are almost identical, with a maximum difference in the predicted elasticity of 0.93 GPa. When comparing the two pole figures, the variance reduction is 99.0 per cent. In this case, the speed of the ANPAR model is 5.8×10^4 greater than that of the SO model (0.384 s for ANPAR versus 2240 s for SO).

6 CONCLUDING REMARKS

The new ANPAR method we describe in this article is an accurate and computationally efficient alternative to existing methods for the simulation of CPO development in olivine. Benchmark tests against the SO self-consistent model (Ponte-Casteñeda 2002) show that ANPAR runs $2\text{--}6 \times 10^4$ times faster, yet predicts textures that are nearly indistinguishable from those predicted by SO. The proposed method is limited to CPO calculations; ANPAR does not tackle the viscoplastic mechanical behaviour of the polycrystal associated with the predicted CPO.

The ANPAR model has some similarities with the D-Rex model of Kaminski & Ribe (2001). In the latter model, the slip rates $\dot{\gamma}^{[s]}$ are predicted by minimizing for each grain the misfit between the local and global SRTs. This *ad hoc* principle yields

$$\dot{\gamma}^{[s]} = 2AS_{ij}^{[s]}E_{ij}, \quad (46)$$

where $A = 1$ if global strain compatibility is not enforced and $A = 5$ if it is. Since the quantities $S_{ij}^{[s]}$ are GSHs of degree 2, D-Rex agrees with ANPAR concerning the spectral content of the crystallographic spin. However, D-Rex assumes that the spin does not depend on the background texture, and so the amplitude A does not increase as strain accumulates. This is in contrast to the amplitudes B and C in ANPAR, both of which increase strongly with increasing strain

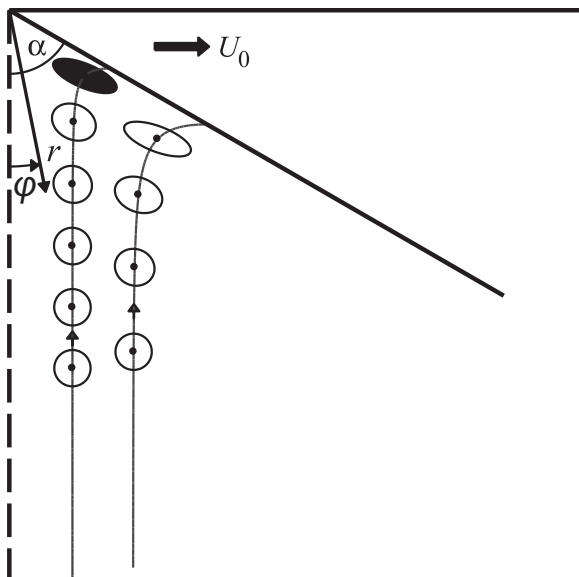


Figure 9. Geometry and boundary conditions for the corner flow model of a ridge crest (right half only). The half spreading rate is U_0 and the asthenospheric wedge has angular dimension $\alpha = 60^\circ$. Solid lines with arrows show typical streamlines for a power-law rheology with index $n = 3$. The FSEs are plotted at different points along the two streamlines. The black ellipse relates to the point in the flow at which the texture is approximated (see Fig. 10).

in order to satisfy global strain compatibility. The ANPAR model for CPO depends on the deformation history, which agrees with the recent studies of Skemer *et al.* (2012) and Boneh & Skemer (2014).

In constructing the ANPAR model we assumed that the spin tensor A_{ijkl} can be written as the product of a tensor Q_{ijkl} that depends only on the axial ratios r_{12} and r_{23} of the FSE and a scalar H that depends only on the relative slip system strengths p_{12} and p_{23} . Although this seems to be a major assumption, the near-perfection of the fits we obtain to the SO predictions appears to justify it.

The simplicity of the ANPAR model is due in part to the orthorhombic symmetry of olivine and the resulting orthogonality of the three dominant slip systems (010)[100], (001)[100] and (010)[001]. This is the reason why the spin consists of only degree-2 GSHs and why the parameter space can be reduced so dramatically. We are investigating the possibility of adapting ANPAR to minerals with non-orthogonal slip systems. We are currently looking at post-perovskite, which is assumed to have slip systems which are aligned with the crystallographic axes plus some slip systems that are oblique to these axes (e.g. Carrez *et al.* 2007a,b; Merkel *et al.* 2007; Metsue *et al.* 2009; Walker *et al.* 2011). For example, $\{110\}[001]$, $(001)\langle 110 \rangle$ and $\{110\}\langle 110 \rangle$ have been proposed as sets of slip systems with symmetry equivalents that are oblique to the crystal axes. In our preliminary investigation it appears that ANPAR can be extended in this manner but the non-orthogonal slip systems result in higher-degree harmonics being required in the model for the crystallographic spin.

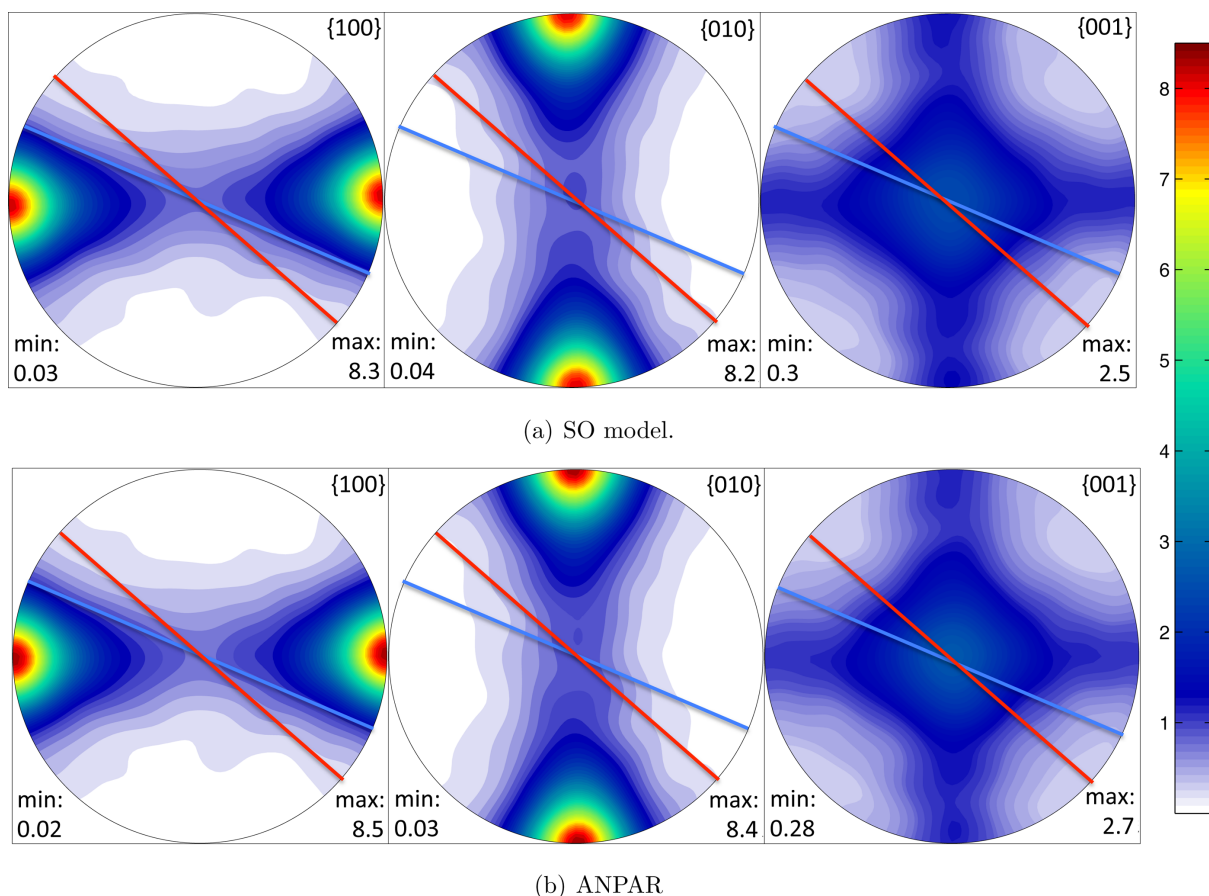


Figure 10. Same as Fig. 6, but for the corner-flow model of a spreading ridge shown in Fig. 9. Textures estimated by the SO and ANPAR models at the point of the filled FSE in Fig. 9. $\alpha = 60^\circ$, $\varphi_0 = 10^\circ$, $\varphi = 49^\circ$, $\chi = 67^\circ$, $r_{12} = 1.047$, $r_{23} = -0.523$ ($r_0 = 0.6$), with CRSS ratios $\tau^{[1]}/\tau^{[2]} = 0.5$ and $\tau^{[2]}/\tau^{[3]} = 0.667$. The red and blue lines have the same meaning as in Fig. 8.

In its current form the ANPAR method does not easily lend itself to modelling polyminerale aggregates; this will be the subject of future development work. However, the model can easily be extended to other orthorhombic minerals with less than four independent slip systems, such as enstatite, and without having to satisfy the von Mises criterion. Detrez *et al.* (2015) show that polycrystalline aggregates lacking four independent systems for dislocation glide can deform in a purely viscoplastic regime only if additional deformation mechanisms (e.g. grain boundary sliding, diffusion, disclinations) are activated, and they assume that the unknown accommodation mechanism can be represented by an isotropic potential. The robust character of our results leads us to suppose that our approach can be generalized to minerals with other symmetries and also to polyphase rocks. If this is the case, the fact that ANPAR is based on the SO model implies that such a generalization could be applicable for a range of materials where first-order homogenization schemes have had limited success and the more computationally taxing SO approach has been considered essential. One such example is modelling of deformation of materials, such as ice, with extreme plastic anisotropy (e.g. Lebensohn *et al.* 2007). Finally, the speed advantage of ANPAR over the SO model holds out the possibility that it could be incorporated efficiently in 3-D and time-dependent simulations of mantle convection.

ACKNOWLEDGEMENTS

The research leading to these results has received funding from the European Research Council under the European Union's Seventh Framework Program (FP7/2007-2013)/ERC grant agreement 240473 CoMITAC. AMW is supported by a fellowship from the Natural Environment Research Council (Grant Number NE/K008803/1). We are grateful to two reviewers whose comments have helped us in clarifying the text and also to A. Nowacki for helpful discussions.

REFERENCES

- Ammann, M.W., Walker, A.M., Stackhouse, S., Forte, A.M., Wookey, J., Brodholt, J.P. & Dobson, D.P., 2014. Variation of thermal conductivity and heat flux at the Earth's core mantle boundary, *Earth planet. Sci. Lett.*, **390**, 175–185.
- Bachmann, F., Hielscher, R. & Schaeben, H., 2010. Texture analysis with MTEX - free and open source software toolbox, *Solid State Phenom.*, **160**, 63–68.
- Bai, Q., Mackwell, S.J. & Kohlstedt, D.L., 1991. High-temperature creep of olivine single crystals. 1. Mechanical results for buffered samples, *J. geophys. Res.*, **96**, 2441–2463.
- Batchelor, G.K., 1967. *An Introduction to Fluid Mechanics*, Cambridge Univ. Press.
- Becker, T., Kustowski, B. & Ekström, G., 2008. Radial seismic anisotropy as a constraint for upper mantle rheology, *Earth planet. Sci. Lett.*, **267**, 213–227.
- Becker, T., Lebedev, S. & Long, M., 2012. On the relationship between azimuthal anisotropy from shear wave splitting and surface wave tomography, *J. geophys. Res.*, **117**, B01306, doi:10.1029/2011JB008705.
- Blackman, D.K., Wenk, H.-R. & Kendall, J.M., 2002. Seismic anisotropy of the upper mantle: 1. Factors that affect mineral texture and effective elastic properties, *Geochem. Geophys. Geosyst.*, **3**, doi:10.1029/2001GC000248.
- Boneh, Y. & Skemer, P., 2014. The effect of deformation history on the evolution of olivine CPO, *Earth planet. Sci. Lett.*, **406**, 213–222.
- Bonnin, M., Tommasi, A., Hassani, R., Chevrot, S., Wookey, J. & Barruol, G., 2012. Numerical modelling of the upper-mantle anisotropy beneath a migrating strike-slip plate boundary: the San Andreas Fault system, *Geophys. J. Int.*, **191**, 436–458.
- Bunge, H.J., 1982. *Texture Analysis in Materials Science*, Butterworths.
- Carrez, P., Ferré, D. & Cordier, P., 2007a. Implications for plastic flow in the deep mantle from modelling dislocations in MgSiO₃ minerals, *Nature*, **446**, 68–70.
- Carrez, P. & Ferré, D. Cordier, P., 2007b. Peierls-Nabarro model for dislocations in MgSiO₃ postperovskite calculated at 120 GPa from first principles, *Phil. Mag.*, **87**, 3229–3247.
- Castelnaud, O., Duval, P., Lebensohn, R.A. & Canova, G.R., 1996. Viscoplastic modelling of texture development in polycrystalline ice with a self-consistent approach: comparison with bound estimates, *J. geophys. Res.*, **101**, 13 851–13 868.
- Castelnaud, O., Canova, G.R., Lebensohn, R.A. & Duval, P., 1997. Modelling viscoplastic behavior of anisotropic polycrystalline ice with a self-consistent approach, *Acta Mater.*, **45**, 4823–4834.
- Castelnaud, O., Blackman, D.K., Lebensohn, R.A. & Castaneda, P.P., 2008. Micromechanical modeling of the viscoplastic behavior of olivine, *J. geophys. Res.*, **113**, B09202, doi:10.1029/2007JB005444.
- Castelnaud, O., Blackman, D.K. & Becker, T.W., 2009. Numerical simulations of texture development and associated rheological anisotropy in regions of complex mantle flow, *Geophys. Res. Lett.*, **36**, L12304, doi:10.1029/2009GL038027.
- Castelnaud, O., Cordier, P., Lebensohn, R., Merkel, S. & Raterron, P., 2010. Microstructures and rheology of the Earth's upper mantle inferred from a multiscale approach, *Comptes Rendus Physique*, **11**, 304–315.
- Chopra, P. & Paterson, M., 1984. The role of water in the deformation of dunite, *J. geophys. Res.*, **89**, 7861–7876.
- Clement, A., 1982. Prediction of deformation texture using a physical principle of conservation, *Mater. Sci. Eng.*, **55**, 203–210.
- Conder, J.A. & Wiens, D.A., 2007. Rapid mantle flow beneath the Tonga volcanic arc, *Earth planet. Sci. Lett.*, **264**, 299–307.
- Cordier, P., 2002. Dislocations and slip systems of mantle minerals, *Rev. Mineral. Geochem.*, **51**, 137–179.
- Cordier, P., Demouchy, S., Beausir, B., Taupin, V., Barou, F. & Fressengeas, C., 2014. Disclinations provide the missing mechanism for deforming olivine-rich rocks in the mantle, *Nature*, **507**, 51–56.
- Cottaar, S., Li, M., McNamara, A.K., Romanowicz, B. & Wenk, H.-R., 2014. Synthetic seismic anisotropy models within a slab impinging on the core–mantle boundary, *Geophys. J. Int.*, **199**, 164–177.
- Crampin, S., 1984. An introduction to wave-propagation in anisotropic media, *Geophys. J. R. astr. Soc.*, **76**, 17–28.
- Deguen, R., Cardin, P., Merkel, S. & Lebensohn, R.A., 2011. Texturing in Earth's inner core due to preferential growth in its equatorial belt, *Phys. Earth planet. Inter.*, **188**, 173–184.
- Detrez, F., Castelnaud, O., Cordier, P., Merkel, S. & Raterron, P., 2015. Effective viscoplastic behavior of polycrystalline aggregates lacking four independent slip systems inferred from homogenization methods; application to olivine, *J. Mech. Phys. Solids*, in press, doi:10.1016/j.jmps.2015.05.022.
- Di Leo, J.F., Walker, A.M., Li, Z.-J., Wookey, J., Ribe, N.M., Kendall, J.-M. & Tommasi, A., 2014. Development of texture and seismic anisotropy during the onset of subduction, *Geochem. Geophys. Geosyst.*, **15**, 192–212.
- Dobson, D.P., Miyajima, N., Nestola, F., Alvaro, M., Casati, N., Liesbke, C., Wood, I.G. & Walker, A.M., 2013. Strong inheritance of texture between perovskite and post-perovskite in the D' layer, *Nat. Geosci.*, **6**(7), 575–578.
- Faccenda, M., 2014. Mid mantle seismic anisotropy around subduction zones, *Phys. Earth planet. Inter.*, **227**, 1–19.
- Faccenda, M. & Capitanio, F.A., 2012. Development of mantle seismic anisotropy during subduction-induced 3-D flow, *Geophys. Res. Lett.*, **39**, L11305, doi:10.1029/2012GL051988.
- Faccenda, M. & Capitanio, F.A., 2013. Seismic anisotropy around subduction zones: insights from three-dimensional modeling of upper mantle deformation and SKS splitting calculations, *Geochem. Geophys. Geosyst.*, **14**, 243–262.
- Grennerat, F., Montagnat, M., Castelnaud, O., Vacher, P., Moulinec, H., Suquet, P. & Duval, P., 2012. Experimental characterization of the intragranular strain field in columnar ice during transient creep, *Acta Mater.*, **60**, 3655–3666.

- Hirth, G. & Kohlstedt, D., 1995. Experimental constraints on the dynamics of the partially molten upper mantle: 2. Deformation in the dislocation creep regime, *J. geophys. Res.*, **100**, 15 441–15 449.
- Jung, H. & Karato, S.-I., 2001. Water-induced fabric transitions in olivine, *Science*, **293**, 1460–1463.
- Kaminski, E. & Ribe, N., 2001. A kinematic model for recrystallization and texture development in olivine polycrystals, *Earth planet. Sci. Lett.*, **189**, 253–267.
- Kaminski, E. & Ribe, N.M., 2002. Time scales for the evolution of seismic anisotropy in mantle flow, *Geochem. Geophys. Geosyst.*, **10**, doi:10.1029/2001GC000222.
- Kaminski, E., Ribe, N.M. & Browaeys, J.T., 2004. D-Rex, a program for calculation of seismic anisotropy in the convective upper mantle, *Geophys. J. Int.*, **158**, 744–752.
- Kanit, T., Forest, S., Galliet, I., Mounoury, V. & Jeulin, D., 2003. Determination of the size of the representative volume element for random composites: statistical and numerical approach, *Int. J. Solids Struct.*, **40**, 3647–3679.
- Kellogg, L.H. & Turcotte, D.L., 1990. Mixing and the distribution of heterogeneities in a chaotically convecting mantle, *J. geophys. Res.*, **95**, 421–432.
- Lachenbruch, A.H. & Nathenson, M., 1974. Rise of a variable viscosity fluid in a steadily spreading wedge-shaped conduit with accreting walls, U.S. Geol. Surv. Open File Rep. 74–251.
- Lassak, T.M., Fouch, M.J., Hall, C.E. & Kaminski, E., 2006. Seismic characterization of mantle flow in subduction systems: Can we resolve a hydrated mantle wedge?, *Earth planet. Sci. Lett.*, **243**, 632–649.
- Lebensohn, R.A., 2001. N-site modeling of a 3D viscoplastic polycrystal using fast Fourier transform, *Acta Mater.*, **49**, 2723–2737.
- Lebensohn, R.A. & Tomé, C.N., 1993. A self-consistent approach for the simulation of plastic deformation and texture development of polycrystals: application to zirconium alloys, *Acta Metall. Mater.*, **41**, 2611–2624.
- Lebensohn, R.A., Tomé, C.N. & Ponte Castañeda, P., 2007. Self-consistent modelling of the mechanical behaviour of viscoplastic polycrystals incorporating intragranular field fluctuations, *Phil. Mag.*, **87**, 4287–4322.
- Lebensohn, R.A., Rollett, A. & Suquet, P., 2011. Fast Fourier Transform-based modelling for the determination of micromechanical fields in polycrystals, *JOM*, **63**, 13–18.
- Lev, E. & Hager, B.H., 2008. Prediction of anisotropy from flow models: A comparison of three methods, *Geochem. Geophys. Geosyst.*, **9**, Q07014, doi:10.1029/2001GC000222.
- Lincot, A., Merkel, S. & Cardin, P., 2015. Is inner core seismic anisotropy a marker for plastic flow of cubic iron?, *Geophys. Res. Lett.*, **42**, 1326–1333.
- Long, M.D., 2013. Constraints on subduction geodynamics from seismic anisotropy, *Rev. Geophys.*, **51**, 76–112.
- Long, M.D. & Becker, T.W., 2010. Mantle dynamics and seismic anisotropy, *Earth planet. Sci. Lett.*, **297**, 341–354.
- Mainprice, D., Tommasi, A., Couvy, H., Cordier, P. & Frost, D., 2005. Pressure sensitivity of olivine slip systems and seismic anisotropy of Earth's upper mantle, *Nature*, **433**, 731–733.
- Mainprice, D., Tommasi, A., Ferré, D., Carrez, P. & Cordier, P., 2008. Predicted glide systems and crystal preferred orientations of polycrystalline silicate Mg-Perovskite at high pressure: implications for the seismic anisotropy in the lower mantle, *Earth planet. Sci. Lett.*, **271**, 135–144.
- McKenzie, D., 1979. Finite deformation during fluid flow, *Geophys. J. R. astr. Soc.*, **58**, 689–715.
- Merkel, S., McNamara, A., Kubo, A., Speziale, S., Miyagi, L., Meng, Y., Duffy, T. & Wenk, H.-R., 2007. Deformation of (Mg,Fe)SiO₃ post-perovskite and D anisotropy, *Science*, **316**, 1729–1732.
- Metsue, A., Carrez, P., Mainprice, D. & Cordier, P., 2009. Numerical modelling of dislocations and deformation mechanisms in CaIrO₃ and MgGeO₃ postperovskites comparison with MgSiO₃ postperovskite, *Phys. Earth planet. Inter.*, **174**, 165–173.
- Molinari, A., Canova, G.R. & Ahzi, S., 1987. A self-consistent approach of the large deformation polycrystal viscoplasticity, *Acta Metall.*, **35**, 2983–2994.
- Montagner, J.-P. & Tanimoto, T., 1991. Global upper mantle tomography of seismic velocities and anisotropies, *J. geophys. Res.*, **96**, 20 337–20 351.
- Moulinec, H. & Suquet, P., 1998. A numerical method for computing the overall response of nonlinear composites with complex microstructure, *Comput. Methods Appl. Mech. Eng.*, **157**, 69–94.
- Muhlhaus, H., Moresi, L. & Cada, M., 2004. Emergent anisotropy and flow alignment in viscous rock, *Pure appl. Geophys.*, **161**, 2451–2463.
- Nicolas, A. & Christensen, N., 1987. Formation of anisotropy in upper mantle peridotites: a review, in composition, structure and dynamics of the lithosphere–asthenosphere system, *Geodyn. Ser.*, **16**, 111–123.
- Nowacki, A., Walker, A.M., Wookey, J. & Kendall, J.-M., 2013. Evaluating post-perovskite as a cause of D' anisotropy in regions of palaeosubduction, *Geophys. J. Int.*, **192**, 1085–1090.
- Ponte Castañeda, P., 2002. Second-order homogenization estimates for nonlinear composites incorporating field fluctuations. I. Theory, and II. Applications, *J. Mech. Phys. Solids*, **50**, 737–782.
- Raterron, P., Detrez, F., Castelnau, O., Bollinger, C., Cordier, P. & Merkel, S., 2014. Multiscale modeling of upper mantle plasticity: from single-crystal rheology to multiphase aggregate deformation, *Phys. Earth planet. Inter.*, **228**, 232–243.
- Ribe, N.M., 1989. Seismic anisotropy and mantle flow, *J. geophys. Res.*, **94**, 4213–4223.
- Ribe, N.M., 1992. On the relation between seismic anisotropy and finite strain, *J. geophys. Res.*, **97**, 8737–8747.
- Ribe, N.M. & Yu, Y., 1991. A theory for plastic deformation and textural evolution of olivine polycrystals, *J. geophys. Res.*, **96**, 8325–8335.
- Sarma, G.B. & Dawson, P.R., 1996. Effects of interactions among crystals on the inhomogeneous deformation of polycrystals, *Acta Mater.*, **44**(5), 1937–1953.
- Silver, P., 1996. Seismic anisotropy beneath the continents: probing the depths of geology, *Annu. Rev. Earth planet. Sci.*, **24**, 385–432.
- Silver, P. & Chan, W., 1991. Shear-wave splitting and subcontinental mantle deformation, *J. geophys. Res.*, **96**, 16 429–16 454.
- Skemer, P., Warren, J.M. & Hirth, G., 2012. The influence of deformation history on the interpretation of seismic anisotropy, *Geochem. Geophys. Geosyst.*, **13**, Q03006, doi:10.1029/2011GC003988.
- Suquet, P., Moulinec, H., Castelnau, O., Montagnat, M., Lahellec, N., Grennerat, F., Duval, P. & Brenner, R., 2012. Multiscale modeling of the mechanical behavior of polycrystalline ice under transient creep, *Procedia IUTAM*, **3**, 64–78.
- Tommasi, A., Tikoff, B. & Vauchez, A., 1999. Upper mantle tectonics: three-dimensional deformation, olivine crystallographic fabrics and seismic properties, *Earth planet. Sci. Lett.*, **168**, 173–186.
- Tommasi, A., Mainprice, D., Canova, G. & Chastel, Y., 2000. Viscoplastic self-consistent and equilibrium-based modeling of olivine lattice preferred orientations: Implications for the upper mantle seismic anisotropy, *J. geophys. Res.*, **105**, 7893–7980.
- Tommasi, A., Mainprice, D., Cordier, P., Thoraval, C. & Couvy, H., 2004. Strain-induced seismic anisotropy of wadsleyite polycrystals and flow patterns in the mantle transition zone, *J. geophys. Res.*, **109**, doi: 10.1029/2004JB003158.
- Tommasi, A., Knoll, M., Vauchez, A., Signorelli, J., Thoraval, C. & Logé, R., 2009. Structural reactivation in plate tectonics controlled by olivine crystal anisotropy, *Nat. Geosci.*, **2**, 423–427.
- Tovish, A., Schubert, G. & Luyendyk, B.P., 1978. Mantle flow pressure and the angle of subduction: non-Newtonian corner flows, *J. geophys. Res.*, **83**, 5892–5898.
- Walker, A.M. & Wookey, J., 2012. MSAT - A new toolkit for the analysis of elastic and seismic anisotropy, *Comput. Geosci.*, **49**, 81–90.
- Walker, A.M., Forte, A.M., Wookey, J., Nowacki, A. & Kendall, J.-M., 2011. Elastic anisotropy of D' predicted from global models of mantle flow, *Geochem. Geophys. Geosyst.*, **12**, Q07014, doi:10.1029/2011GC003732.
- Wenk, H.-R. & Tomé, C.N., 1999. Modeling dynamic recrystallization of olivine aggregates deformed in simple shear, *J. geophys. Res.*, **104**, 25513–25527.

- Wenk, H.-R., Bennett, K., Canova, G.R. & Molinari, A., 1991. Modelling plastic deformation of peridotite with the self-consistent theory, *J. geophys. Res.*, **96**, 8337–8349.
- Wenk, H.-R., Baumgardner, J.R., Lebensohn, R.A. & Tomé, C.N., 2000. A convection model to explain anisotropy of the inner core, *J. geophys. Res.*, **105**, 5663–5677.

- Wenk, H.-R., Speziale, S., McNamara, A. & Garnero, E., 2006. Modeling lower mantle anisotropy development in a subducting slab, *Earth planet. Sci. Lett.*, **245**, 302–314.
- Wenk, H.-R., Cottaar, S., Tomé, C.N., McNamara, A. & Romanowicz, B., 2011. Deformation in the lowermost mantle: from polycrystal plasticity to seismic anisotropy, *Earth planet. Sci. Lett.*, **306**, 33–45.

APPENDIX A: SLIP SYSTEM-SPECIFIC SCHMID TENSORS

The Schmid tensor \mathbf{S} is slip system specific, and thus different for each system. Let $S_{ij}^{[s]}$ be the Schmid tensor for slip system s . For the slip system (010)[100] ($s = 1$), the relationships between the independent components of the Schmid tensor and the Eulerian angles are

$$S_{11}^{[1]} - S_{22}^{[1]} = -\frac{1}{2} [\cos 2\phi \sin 2\psi (\cos^2 \theta + 1) + 2 \sin 2\phi \cos \theta \cos 2\psi], \quad (\text{A1a})$$

$$S_{12}^{[1]} = -\frac{1}{4} [\sin 2\phi \sin 2\psi (\cos^2 \theta + 1) - 2 \cos 2\phi \cos \theta \cos 2\psi], \quad (\text{A1b})$$

$$S_{13}^{[1]} = -\frac{1}{2} \sin \theta (\sin \phi \cos \theta \sin 2\psi - \cos \phi \cos 2\psi), \quad (\text{A1c})$$

$$S_{23}^{[1]} = \frac{1}{2} \sin \theta (\cos \phi \cos \theta \sin 2\psi + \sin \phi \cos 2\psi), \quad (\text{A1d})$$

$$S_{11}^{[1]} + S_{22}^{[1]} = -\frac{1}{2} \sin^2 \theta \sin 2\psi. \quad (\text{A1e})$$

Similarly, for the slip system (001)[100] ($s = 2$) we obtain

$$S_{11}^{[2]} - S_{22}^{[2]} = \sin \theta (\cos 2\phi \cos \theta \sin \psi + \sin 2\phi \cos \psi), \quad (\text{A2a})$$

$$S_{12}^{[2]} = \frac{1}{2} \sin \theta (\sin 2\phi \cos \theta \sin \psi - \cos 2\phi \cos \psi), \quad (\text{A2b})$$

$$S_{13}^{[2]} = -\frac{1}{2} (\sin \phi \cos 2\theta \sin \psi - \cos \phi \cos \theta \cos \psi), \quad (\text{A2c})$$

$$S_{23}^{[2]} = \frac{1}{2} (\cos \phi \cos 2\theta \sin \psi + \sin \phi \cos \theta \cos \psi), \quad (\text{A2d})$$

$$S_{11}^{[2]} + S_{22}^{[2]} = -\frac{1}{2} \sin 2\theta \sin \psi. \quad (\text{A2e})$$

Finally, for the slip system (010)[001] ($s = 3$) we find

$$S_{11}^{[3]} - S_{22}^{[3]} = \sin \theta (\cos 2\phi \cos \theta \cos \psi - \sin 2\phi \sin \psi), \quad (\text{A3a})$$

$$S_{12}^{[3]} = \frac{1}{2} \sin \theta (\sin 2\phi \cos \theta \cos \psi + \cos 2\phi \sin \psi), \quad (\text{A3b})$$

$$S_{13}^{[3]} = -\frac{1}{2} (\sin \phi \cos 2\theta \cos \psi + \cos \phi \cos \theta \sin \psi), \quad (\text{A3c})$$

$$S_{23}^{[3]} = \frac{1}{2} (\cos \phi \cos 2\theta \cos \psi - \sin \phi \cos \theta \sin \psi), \quad (\text{A3d})$$

$$S_{11}^{[3]} + S_{22}^{[3]} = -\frac{1}{2} \sin 2\theta \cos \psi. \quad (\text{A3e})$$

APPENDIX B: AMPLITUDE OF THE CRYSTALLOGRAPHIC ROTATION RATE

In this appendix, we quantify the dependence of the slip system amplitudes $A_{ijkl}^{[s]}$ on the strains r_{12} and r_{23} and the CRSS ratios p_{12} and p_{23} . We assume that \mathbf{A} can be expressed more compactly, as shown in eq. (23).

Table B1. Values of the coefficients z_{mn} in the fitting functions (B3), for $B(r_{12}, r_{23})$ and $C(r_{12}, r_{23})$.

	z_{00}	z_{20}	z_{11}	z_{02}	z_{40}	z_{31}	z_{22}	z_{13}	z_{04}
B	2.241	0.3993	1.104	1.104	0.7619	2.507	5.518	6.023	3.012
C	1.662	0.2046	0.1992	-0.7517	-0.01853	-0.02831	-0.4396	-0.4246	0.2085

B1 Limit $A_{ijkl}^{[s]}(r_{12}, r_{23}, \mathbf{0}, \mathbf{0}, 3.5)$

We first consider how the activities of slip systems with equal strengths ($p_{12} = p_{23} = 0$) vary as a function of strain. This enables us to find out how the Q_{ijkl} depend on the parameters r_{12} and r_{23} that characterize the FSE. As we pointed out in Section 2.3, the value of $m = 3.5$ is assumed for all slip systems.

We explained in Section 4.2 the symmetries that allow us to reduce the number of independent non-zero components Q_{ijkl} from 25 to just 2. The transformation rules (24), derived by noting that the labelling of the coordinate axes is arbitrary, are given in their full form here:

$$Q_{1212}(r_{12}, r_{23}) = C(r_{12}, r_{23}) = C(-r_{12}, -r_{23}) = C(r_{12}, r_{31}) = C(-r_{12}, -r_{31}), \quad (\text{B1a})$$

$$Q_{1313}(r_{12}, r_{23}) = C(r_{31}, r_{12}) = C(-r_{31}, -r_{12}) = C(r_{31}, r_{23}) = C(-r_{31}, -r_{23}), \quad (\text{B1b})$$

$$Q_{2323}(r_{12}, r_{23}) = C(r_{23}, r_{31}) = C(-r_{23}, -r_{31}) = C(r_{23}, r_{12}) = C(-r_{23}, -r_{12}), \quad (\text{B1c})$$

$$Q_{1111}(r_{12}, r_{23}) = B(r_{12}, r_{23}) = B(-r_{12}, -r_{23}) = B(r_{31}, r_{23}) = B(-r_{31}, -r_{23}), \quad (\text{B1d})$$

$$Q_{2222}(r_{12}, r_{23}) = B(r_{12}, r_{31}) = B(-r_{12}, -r_{31}) = B(r_{23}, r_{31}) = B(-r_{23}, -r_{31}), \quad (\text{B1e})$$

$$\begin{aligned} B(r_{31}, r_{12}) &= B(-r_{31}, -r_{12}) = B(r_{23}, r_{12}) = B(-r_{23}, -r_{12}) \\ &= B(r_{12}, r_{23}) + 2Q_{1122}(r_{12}, r_{23}) + Q_{2222}(r_{12}, r_{23}). \end{aligned} \quad (\text{B1f})$$

We also discovered, numerically, the symmetry condition

$$Q_{ijkl}(r_{12}, r_{23}) = Q_{ijkl}(-r_{12}, -r_{23}). \quad (\text{B2})$$

This means, for example, that the values of Q_{ijkl} for uniaxial extension are identical to those for uniaxial compression. Using eq. (B2) and the complete symmetry transformations (B1), we can reduce by a factor of eight the size of the parameter space (r_{12}, r_{23}) that we have to explore numerically to determine how B and C depend on r_{12} and r_{23} .

We determine values of B and C at sampled points in the (r_{12}, r_{23}) -plane by fitting eq. (26) (with $H^{[s]}(0, 0) = 1$) to the spin predicted by the SO model, using a standard least-squares procedure. These calculations yield the curves shown by solid lines in Figs 4 and 5. In each case the variance reduction $R > 99.7$ per cent. Then, we fitted B and C data, obtained by the above method, to fourth-order polynomials of the form

$$\sum_{m=0}^4 \sum_{n=0}^4 z_{mn} r_{23}^m r_{12}^n, \quad (\text{B3})$$

where

$$z_{mn} = \begin{cases} 0 & \text{if } m + n > 4; \\ 0 & \text{if } m + n \text{ odd}; \\ z_{mn} & \text{otherwise.} \end{cases} \quad (\text{B4})$$

The RMS errors of the fits to the B and C data are 0.039 and 0.0070, respectively. The values of the non-zero coefficients z_{mn} are given in Table B1, for both fitting functions. The quality of these fits can be viewed in Figs 4 and 5.

B2 Limit $A_{ijkl}^{[s]}(\mathbf{0}, \mathbf{0}, p_{12}, p_{23}, 3.5)$

We next consider how the amplitudes depend on p_{12} and p_{23} at the initial instant ($r_0 = r_{12} = r_{23} = 0$) of the deformation. This allows us to discover how the functions $H^{[s]}$ in eq. (23) depend on the parameters that characterize the relative strength of the slip systems. Here, we consider values of p_{12} and p_{23} in the range $[-\ln 4, \ln 4] \approx [-1.386, 1.386]$. We discovered numerically the following transformation rules:

$$H^{[1]}(p_{12}, p_{23}) = H^{[1]}(-p_{31}, -p_{23}) \quad (\text{B5a})$$

$$H^{[2]}(p_{12}, p_{23}) = H^{[1]}(-p_{12}, -p_{31}) = H^{[1]}(p_{23}, p_{31}) \quad (\text{B5b})$$

$$H^{[3]}(p_{12}, p_{23}) = H^{[1]}(-p_{23}, -p_{12}) = H^{[1]}(p_{31}, p_{12}). \quad (\text{B5c})$$

These transformations enable us not only to express $H^{[2]}$ and $H^{[3]}$ in terms of $H^{[1]}$, but also to reduce the size of the parameter space (p_{12}, p_{23}) that we have to explore numerically to determine how $H^{[1]}$ depends on p_{12} and p_{23} .

We obtain $H^{[1]}$ data by calculating, via least-squares, the amplitudes $H^{[1]}$ that fit eq. (26) to 81 instantaneous numerical solutions of the SO model for uniaxial compression, with equally spaced points in the (p_{12}, p_{23}) -plane with both p_{12} and p_{23} in the range $[-1.386, 1.386]$. We then fit quadratic polynomials, satisfying the above relations (B5), to the collected $H^{[1]}$ data. The results are

$$H^{[1]}(p_{12}, p_{23}) = 1 - 0.0295p_{12} - 0.0130p_{23} - 0.00743p_{12}^2 - 0.00347p_{12}p_{23} - 0.00333p_{23}^2. \quad (\text{B6})$$

The RMS error of the fit is 0.0068. We apply the transformations (B5) to form analytical expressions for $H^{[2]}$ and $H^{[3]}$, respectively.

B3 General case

We construct a general form for $A_{ijkl}^{[s]}(r_{12}, r_{23}, p_{12}, p_{23})$ that is consistent with the above limiting cases. We first substitute the model (B6) into eq. (23). We then use the coefficients in eq. (B4) and Table B1 to formulate the models (B3) for *B* and *C*. The *B* and *C* models are substituted into eqs (24a)–(24f) to form Q_{ijkl} , which is subsequently used in eq. (23). The resulting expression is the one we use in all our numerical calculations.

We have fitted this model to the spin predicted by the SO model for random background textures (formed using various r_{12} , r_{23} , p_{12} and p_{23} values) and random instantaneous SRT's. Remarkably, in each case, the variance reduction $R > 99.1$ per cent and in most cases $R > 99.7$ per cent.

APPENDIX C: VARIANCE REDUCTION BETWEEN POLE FIGURES

To calculate the variance reduction between the pole figures shown in Section 5, we use the transformations

$$\phi_n^* = \frac{2}{\pi}\phi_n, \quad \theta_n^* = 1 + \cos\theta_n, \quad \psi_n^* = \frac{2}{\pi}\psi_n \quad (\text{C1})$$

to map the Euler angles $(\phi_n, \theta_n, \psi_n)$ of each grain onto an 'Euler cube' $(\phi_n^*, \theta_n^*, \psi_n^*)$. The Euler cube has a uniform metric, and each of its sides is of length 2.0. Let the set of Euler angles for each grain for the SO and ANPAR approximations be denoted by $(\phi_{(n,\text{SO})}^*, \theta_{(n,\text{SO})}^*, \psi_{(n,\text{SO})}^*)$ and $(\phi_{(n,\text{AN})}^*, \theta_{(n,\text{AN})}^*, \psi_{(n,\text{AN})}^*)$, respectively. For each grain the 'distance', d_n , between these two sets of Euler angles is calculated by

$$d_n = \sqrt{\left(\phi_{(n,\text{SO})}^* - \phi_{(n,\text{AN})}^*\right)^2 + \left(\theta_{(n,\text{SO})}^* - \theta_{(n,\text{AN})}^*\right)^2 + \left(\psi_{(n,\text{SO})}^* - \psi_{(n,\text{AN})}^*\right)^2}. \quad (\text{C2})$$

The variance reduction between the two pole figures is then given by

$$R = 1 - \frac{\sum_{n=1}^N d_n^2}{\sum_{n=1}^N \left[\left(\phi_{(n,\text{SO})}^*\right)^2 + \left(\theta_{(n,\text{SO})}^*\right)^2 + \left(\psi_{(n,\text{SO})}^*\right)^2 \right]}. \quad (\text{C3})$$